

SIMULATIONS AND PROTOTYPING OF AN MPGD AND A WIRE-BASED DETECTOR

A Project Report Submitted
in Partial Fulfilment of the Requirements
for the Degree of

MASTER OF SCIENCE

by

S Danush



To

National Institute of Science Education and Research (NISER).

At - Bhimpur, Padanpur, PO - Jatani,

Dist - Khordha – 752050, Odisha, India

DECLARATION

I, along with my undersigned Guide, are co-owners of the copyright of this thesis/dissertation. NISER is hereby granted, exclusive, royalty-free, and non-transferable rights to make available, in full or in part without any modification, this thesis/dissertation in electronic/printed form solely for academic use at no charge. Any use of material from this thesis/dissertation must be accompanied with appropriate citation and prior permission. This thesis/dissertation is not covered under creative commons license.

Date:

Signature of Student

The thesis work reported in the thesis entitled **Simulations and Prototyping of an MPGD and a Wire-Based Detector** was carried out under my supervision, in the **School of Physical Sciences** at NISER, Bhubaneswar, India.

Signature of Thesis Supervisor

School:

Date:

ACKNOWLEDGEMENTS

My first thanks go to Prof. Bedangadas Mohanty for providing me the opportunity to work under his guidance on this project and for teaching me a lot of things in science and life in general. I could not have asked for a better guide and mentor for this project.

I thank Dr. Varchaswi K S Kashyap, Dr. Shuddha Shankar Dasgupta, and Dr. Ajit Kumar for their supervision and for bearing a lot of my amateur doubts I have asked during these past couple of months.

I would like to extend my thanks to the Robotics lab, Dr. Subhankar Mishra, Mr. Jyothish Kumar, Mr. Oommen P Jose, and Mr. Shriman Keshri for letting us use the 3D printer and for getting the prints done during odd hours. I thank Mr. Subasha Rout for his help with electronics and the mechanical engineering tasks we were involved in. His experience and knowledge with circuits are extraordinary.

I thank Dr. Ganesh Jagannath Tambave, Dr. Raveendrababu Karnam, Mr. Ashish Pandav (one of those lakh guldastas), Mr. Debasish Mallick, Mr. Dukhishyam Mallick, Ms. Mouli Chaudhuri, Mr. Prottay Das, Mr. Sudipta Das, and Ms. Swati Saha for making the lab environment memorable, and I proudly say this, the best amongst all of SPS.

I would like to thank Ms. Adishree M, Mr. Akilan K, Mr. Aman Upadhyay, Mr. Chinmay Routray, and Mr. Nisarg Vyas for all the cherishable conversations and for bearing my attitude when deadlines were looming over.

I finally am grateful to my parents and sister for the patience and ever-showering love during all the times I hadn't called them.

ABSTRACT

Gas detectors form an important part of a larger detector in experiments at facilities like those at the Large Hadron Collider (LHC) and Relativistic Heavy Ion Collider (RHIC). There are also applications in fields like medical imaging, and thus an understanding of such devices can help improve science's impact on society. This project involves studying the interaction of radiation and particles with matter, concepts that are crucial to understanding the science behind gas detectors, with a focus on the Thick-GEM detector (a Micro Pattern Gaseous Detector) and the proportional counter (a wire-based detector). We designed, fabricated, and characterized a Thick-GEM detector and a proportional counter. We characterized both detectors using an ^{55}Fe source, wherein for the Thick-GEM detector, we studied the variation of gain with the voltage bias across the foil, and the variation of count rate with the drift and induction fields; and for the proportional counter, we studied the variation of gain with the voltage given to the anode. We also performed a study on the gain evolution upon sustained exposure to radiation for both detectors. Simulations were also done using Garfield++ and the neBEM library to get more insight into the working principles of these detectors.

Contents

1	Outline	1
2	Energy Loss of Particles in Matter	2
2.1	Interaction of Charged Particles With Matter	2
2.2	Interaction of Photons With Matter	4
2.3	Interaction of Neutrons With Matter	5
3	Introduction to Gaseous Detectors	7
3.1	Physical Processes in Gaseous Detectors	7
3.1.1	Mobility of Charge Carriers	7
3.1.2	Avalanche Multiplication	8
3.2	Modes of Operation	8
3.3	Proportional Counter	10
3.4	Multi-Wire Proportional Counter	12
3.5	Micro-Strip Gaseous Chamber	12
3.6	Micro Mesh Gaseous Detector	13
3.7	Gas Electron Multipliers	14
3.8	Thick-Gaseous Electron Multipliers	16
4	Development of the Thick-GEM Detector	18
4.1	Overview	18
4.2	PCB and Readout Strips	22
4.3	Drift Electrode	22
4.4	Gas-Tight Enclosure	24
4.5	Assembly in a Clean Room	26
4.6	Gas Selection and Quenching Gases	27
4.7	Electronics Used	27
4.7.1	Preamplifier	28
4.7.2	Spectroscopic Amplifier	28

4.7.3	Multi-Channel Analyser	30
4.8	Preliminary Tests	30
4.9	Measuring the Energy Spectrum of ^{55}Fe Source	30
4.10	Components Check	31
4.11	Study on the Expected Output	32
4.11.1	Simulation of Expected Gain	34
4.12	Noise Reduction	40
4.13	Reducing Leak Current	42
4.14	Increasing Signal Amplitude	44
4.15	Characterization of the Thick-GEM Detector	46
4.16	Gain Evolution in the Thick-GEM Detector	48
5	Development of the Proportional Counter	50
5.1	Overview	50
5.2	Design and Fabrication	51
5.3	Initial Checks	52
5.4	Characterization of the Proportional Counter	53
5.5	Operating at Negative Voltage	54
5.6	Gain Evolution in the Proportional Counter	56
6	Conclusion and Outlook	59
	Bibliography	60
	Appendix A Derivations	63
A.1	Bohr's Derivation of Energy Loss of Heavy Particles in Matter	63
A.2	Interaction Probability and Mean Free Path	65
A.3	Signal Induced in a Proportional Counter	66
	Appendix B The Code for Simulating the Thick-GEM Detector on Garfield++	68
	Appendix C The Code for Simulating the Proportional Counter	93

List of Figures

2.1	Total photon absorption cross-section for Aluminium. Source: https://physics.nist.gov/PhysRefData/Xcom/html/xcom1.html	5
3.1	Modes of operation of a gas detector. Source: https://www.intechopen.com/chapters/48796	9
3.2	Schematic diagram of a proportional counter.	11
3.3	A cross-sectional schematic diagram of an MWPC.	12
3.4	(a) A schematic cross-sectional diagram of the MSGC with typical dimensions. (b) The electric field lines of the MSGC. Source: [5]	13
3.5	Schematic diagram of the micromegas detector. Source: https://iopscience.iop.org/article/10.1088/1748-0221/7/03/C03040	14
3.6	(a) A top view image of the GEM foil. (b) The electric field lines across a GEM hole. Source: [6]	15
3.7	Cross-section schematic of the GEM and Thick-GEM holes (Not to scale). .	16
4.1	A cross-sectional schematic diagram of the detector and the electronic circuits used.	19
4.2	Isometric view of the design of the detector made using AutoCAD.	20
4.3	Second isometric view of the detector.	20
4.4	Top view of the detector showing the two electrodes and the Thick-GEM Foil.	21
4.5	The PCB with the readout strips and other terminals after the chemical etching process. Four holes were also drilled, which will be used to hold the Thick-GEM foil and the drift electrode.	23
4.6	(a) The frame of the drift electrode and (b) an image of the fully-constructed drift electrode.	23
4.7	(a) The Perspex frame with the inlet and outlet valves. (b) The rubber layer that will be placed on top of the Perspex layer to act as a seal for the joint. (c) A zoomed-in image of the top enclosure to show the ridge.	25

4.8	(a) An O-ring sealed vacuum connection (Source: [11]). (b) An image of the detector after the placement of the Perspex walls and installation of screws taped with Teflon to prevent gas leaks. (c) Image of the top enclosure.	25
4.9	Gas leak rate for the (a) first attempt and (b) second attempt (tighter joint).	26
4.10	A circuit diagram of a typical charge-sensitive preamplifier. This figure shows how a typical input pulse and output look like. Source: [12]	28
4.11	A schematic diagram of the input pulse to the amplifier and the output pulse. The inter. We see that the output pulse has been shaped, which is done through a shaping circuit. Source: [13]	29
4.12	The schematic diagram of a typical shaping circuit. Source: [14]	29
4.13	The outputs of a CR-RC shaping circuit to a step voltage. Curves are shown for several different combinations of time constants and are labeled as (time constant of CR circuit + time constant of RC circuit). Source: [14]	29
4.14	The square pulse generated by the pulse generator.	32
4.15	The square pulse after being shaped by the RC-shaping circuit.	32
4.16	The preamplifier output for the input pulse shown in Figure 4.15.	32
4.17	Computed first Townsend coefficient as a function of the electric field in several gases at NTP. Source [16]	33
4.18	An image of the unit cell of the Thick-GEM setup.	35
4.19	A plot of equi-potential lines (a) across the Thick-GEM foil (across three holes) and (b) across the full detector. The legend on the right for both images are potential values (in V). This was for 20 copies of the unit cell along X and Y directions each.	36
4.20	(a) An image of the unit cell of the Thick-GEM setup with a new pitch. (b) A plot of equi-potential lines across the Thick-GEM foil (across three holes). The legend on the right for both images are potential values (in V). This was for 20 copies of the unit cell along X and Y directions each.	36
4.21	(a) Contour plot of the electric field across the XY-plane in the center of the Thick-GEM foil (35 kV/cm). (b) Electric field values across a line in the center of the hole parallel to the X-axis.	38

4.22	A plot of collection and extraction efficiency for different $E_{\text{drift}}/E_{\text{hole}}$ values. This simulation was done for two different E_{hole} values (25 and 30 kV/cm) and three different E_{drift} values (1, 2, and 3 kV/cm). The coordinates in the plots adjacent to the points correspond to ($E_{\text{drift}}/E_{\text{hole}}$, CE or EE).	39
4.23	(a) An image of the detector inside the Faraday's cage. (b) A view of the detector inside the Faraday's cage.	39
4.24	(a) The schematic circuit diagram to measure noise from the preamplifier connected to readout strips of the detector and (b) the corresponding output of the preamplifier.	40
4.25	Images of the detector setup after steps were taken to reduce noise.	41
4.26	Noise observed from the preamplifier at different stages of attempts to reduce the noise. A noise of about 15 mV is seen in (a) and about 6 mV in (b).	41
4.27	The noise observed from the detector (less than 2 mV). The circuit diagram of the setup in consideration would be similar to that of Figure 4.24a but with the detector output directly connected to the oscilloscope.	42
4.28	Images of (a) front side and (b) backside of the well-soldered and cleaned protective circuit made in a way to have minimum leakage in current.	43
4.29	For an ^{55}Fe source, the output from the (a) preamplifier and (b) amplifier that was observed with an oscilloscope. Here the X-Axis is the time, and the Y-Axis is the voltage.	45
4.30	The MCA output for an ^{55}Fe source placed in front of the Thick-GEM detector. Here the X-Axis is the channel number, and the Y-Axis is the counts.	45
4.31	A plot of the effective gain vs. voltage bias across the Thick-GEM foil.	46
4.32	A plot of resolution vs. voltage bias across the Thick-GEM foil.	47
4.33	Plots of the variation of count rate with the (a) drift and (b) induction fields.	48
4.34	The shift in the peak of the MCA spectrums obtained at two different times during the continuous exposure to radiation. The shift in centroid shows the drop in the detector gain over time.	49
4.35	The evolution of gain over time for the Thick-GEM detector.	49
5.1	Image of (a) the end cap designed on AutoCAD and (b) the 3D printed end caps.	51

5.2	An image of (a) the proportional counter built and (b) the detector placed in a Faraday cage.	52
5.3	For an ^{55}Fe source, the output from the (a) preamplifier and (b) amplifier that was observed with an oscilloscope. Here the X-Axis is the time, and the Y-Axis is the voltage.	53
5.4	The MCA output for an ^{55}Fe source placed in front of the proportional counter. Here the X-Axis is the channel number, and the Y-Axis is the counts.	53
5.5	The plot of resolution vs. voltage applied to the anode wire.	54
5.6	An image captured when the proportional counter was sparking.	54
5.7	For an ^{55}Fe source, the preamplifier output of the proportional counter in the negative-voltage configuration. Here the X-Axis is the time, and the Y-Axis is the voltage.	55
5.8	The shift in the peak of the MCA spectrums obtained at two different times during the continuous exposure to radiation. The shift in centroid shows the drop in the detector gain over time.	57
5.9	A plot of the variation of gain with time to demonstrate the drop in gain in the proportional counter upon continuous radiation exposure.	58
A.1	Schematic diagram of the collision of the incident particle and an electron bound to the atoms of the material. Source: [1]	63

List of Tables

3.1	Comparison of some specifications between a typical GEM and Thick-GEM foil.	17
4.1	Typical potentials that are supplied to each electrode in the detector.	21
4.2	Dimensions and electric field magnitudes for different regions in the detector	21
4.3	Voltages applied to the electrodes.	35
4.4	The results of the simulated gain values for different electric fields in the Thick-GEM hole region (E_{hole}).	37
4.5	The leak current in the circuits for the three terminals for the corresponding voltage applied. I_{bottom} , I_{top} , and I_{drift} correspond to the current in the lower Thick-GEM, upper Thick-GEM, and drift electrode circuits, respectively. . .	43
4.6	The leak current in the circuits after careful construction and precautions. An image of the corresponding circuit is as seen in 4.28. The values marked in red are above the accepted limit.	43
4.7	The leak current in the circuits after the removal of the low pass filter. . . .	44

Chapter 1

Outline

This thesis has been divided into four chapters. Chapter 2 discusses the study of energy loss of particles that traverses through matter. These are concepts that are employed and taken advantage of by detectors in most high energy physics experiments. The chapter then goes into some pre-requisites to understand the microscopic processes that occur in gaseous detectors. Chapter 3 introduces the history of gaseous detectors, the need for such detectors, and some details on Gas Electron Multipliers (GEMs) and Thick-GEMs. We try to capture how the journey of the development of gas detectors brought us to where we are now with new detectors like the Thick-GEM detector. Chapter 4 describes the design and efforts taken to fabricate all components of the Thick-GEM detector, in India. We then discuss the preliminary tests, characterization studies, and their subsequent results. Chapter 5 describes the fabrication process of the proportional counter, the tests conducted, and subsequent results. Finally, Chapter 6 concludes this thesis.

Chapter 2

Energy Loss of Particles in Matter

A crucial objective in most nuclear or particle physics experiments is the detection of radiation and particles. It is thus essential to look at how different particles and radiation interact with matter. These interactions can be classified into two types based on whether the incident particle is a photon or a charged particle. Information like the energy and position of an incoming particle can be extracted based on information we obtain from these interactions.

2.1 Interaction of Charged Particles With Matter

A charged particle traversing through matter can be characterized by the following interactions it can undergo with the atoms/molecules of the medium [1]:

1. Inelastic collisions with atomic electrons of the medium
2. Elastic scattering with the nuclei of the medium
3. Emission of Cherenkov radiation
4. Nuclear reactions
5. Bremsstrahlung

As explained in [1], inelastic collisions with electrons of the medium and the incident particle involve the excitation or ionization of these electrons, and although the energy lost by the incident particle is not a lot for one such collision, it adds up to a considerable number in the end, because of the total number of such collisions that usually take place. Elastic collisions with the nuclei of the medium do not take place as often as inelastic collisions with the electrons of the medium, and these types of collisions do not account for the majority of energy loss of the incident particle. The other three effects also are possible but are less frequent than the first two.

It is useful to calculate the amount of energy lost by an incoming particle as it traverses through a medium, and it was the seminal work of Niels Bohr, Hans Bethe, and Felix Bloch, among others, that paved the way for these calculations. The information from these calculations formed the foundations based on which we built detectors that can now help us identify the (charged) particle and calculate the energy with which they hit the detector. Although Bohr derived the stopping power (mean energy lost per unit path length) for heavy charged particles using classical arguments, it was Bethe and Bloch that performed the same using quantum mechanics. The derivation by Bohr is explained in Appendix A.1.

The Bethe-Bloch equation describes the energy loss (through many interactions) that heavy-charged particles like alpha particles undergo while traversing through a medium. The equation is as follows:

$$-\frac{dE}{dx} = 2\pi N_a r_e^2 m_e c^2 \rho \frac{Z}{A} \frac{z^2}{\beta^2} \left[\ln \left(\frac{2m_e \gamma^2 v^2 W_{\max}}{I^2} \right) - 2\beta^2 - \delta - 2\frac{C}{Z} \right], \quad (2.1)$$

where r_e and m_e are the radius and mass of an electron respectively, N_a is the Avogadro's number, I is the mean excitation potential, Z , A , and ρ are the atomic number, atomic weight, and density of the medium respectively, z and v are the charge and velocity of the incident particle respectively, δ and C are the density and shell correction terms respectively and W_{\max} is the maximum energy transfer possible in a single collision (obtained from kinematics).

The expressions obtained by Bohr and Bethe-Bloch arise from classical and quantum mechanical frameworks, respectively. However, it is also to be noted that apart from the correction terms, the final equations have the same dependence on z , Z , A , ρ , and differ in v by one degree. (Here, degree means the power of the variable. Eg. - degree of x in x^3 is 3.) Bohr's result is pretty accurate, considering it was derived from a classical picture.

The density correction term is required to deal with the polarisation that the incident particle can bring about in the atoms of the medium along its path. Due to this, the electrons further away from this path will experience a shielding from the true electric field intensity of the incident particle. The Bethe-Bloch equation would break down if the velocity of the incident particle is comparable to or lower than the orbital velocity of the bound electrons of the atoms of the medium. This is because the equation assumes that the electrons of the medium are stationary with respect to the incident particle. The shell corrections precisely look into this aspect. It accounts for effects that arise when the velocity of the incident

particle is low.

We see that the Bethe-Bloch equation is initially dominated by the β^2 term, so there is a drop in dE/dx as the energy of the incident particle increases. At higher energies, the logarithmic term starts to weigh in, thus increasing dE/dx and ideally should keep on increasing as the energy of the incident particle also increases, but this rise is canceled due to the density correction term [1].

We mentioned that, to apply the Bethe-Bloch equation, the incident particle has to be a heavy charged particle, and electrons and positrons are light charged particles. This condition exists because the derivation involves assuming that the incident particle remains undeflected as it traverses through the medium. With electrons, we also arrive at the indistinguishability problem when it collides with other electrons of the medium. But one can still modify the Bethe-Bloch equation to obtain an equation for stopping power [1]. Additionally, Bremsstrahlung also has to be factored in to calculate energy loss through the same process.

2.2 Interaction of Photons With Matter

The interaction of photons with matter happens majorly through the Photoelectric effect, the Compton Effect, and the Pair-Production Effect. Depending on the properties like the incident energy of the photon, the cross-sections of each of these processes vary.

The photoelectric effect refers to the emission of electrons when a photon interacts with it. It occurs when the energy of the incident photon is higher but around the magnitude of the atom's ionization energy. Sometimes the photon can eject an inner shell electron followed by rearrangement of electrons in the atom producing another photon or electron during the process.

The Compton effect occurs when the energy of the incident photon is to some extent more significant than the ionization energy of the atom. It is the process of transferring some of the energy and momentum to an electron the photon collides with. Similar to Compton scattering, we also have Thomson and Rayleigh scattering. Thomson scattering is the scattering of photons by free electrons, but in the classical limit (low energies). Rayleigh scattering is the scattering of photons by atoms acting as an entity.

The Pair-Production effect is observed when the incident photon is of energy greater than twice the mass of an electron. Pair production often refers to a photon creating an

electron-positron pair near a nucleus.

As explained, the above processes come into the picture at different energies of the incident particle. In more rigorous terms, the cross-sections of the above processes vary with different energies of the incident particle. Figure 2.1 is an example of the same. Note that coherent scattering is another name given to Thomson scattering and incoherent scattering is Compton scattering.

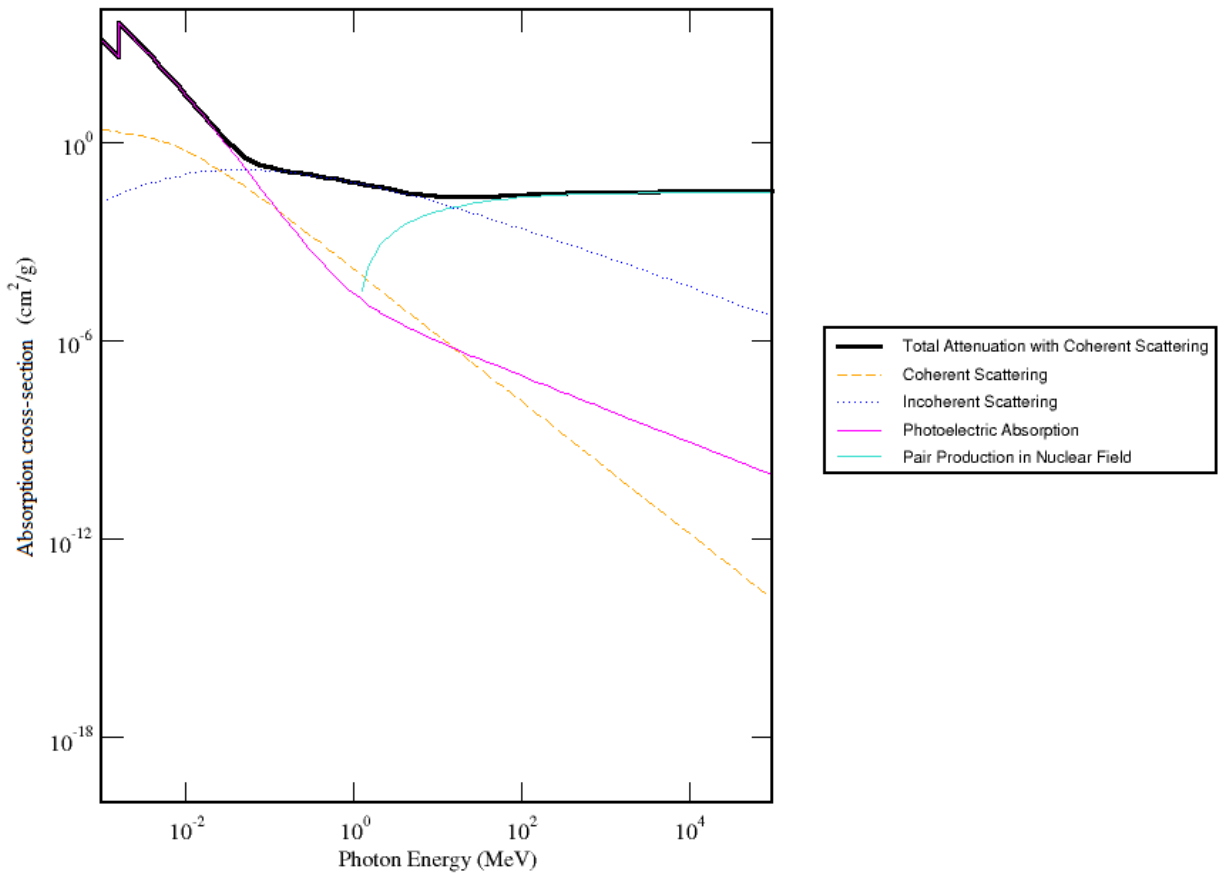


Figure 2.1: Total photon absorption cross-section for Aluminium. Source: <https://physics.nist.gov/PhysRefData/Xcom/html/xcom1.html>.

2.3 Interaction of Neutrons With Matter

Neutrons are particles with no charge and hence are not involved in any electromagnetic interaction with charged particles at the energies we are concerned with. However, they can

interact with other nuclei through the following processes [1]:

1. Radioactive neutron capture
2. Fission
3. Elastic and inelastic scattering from nuclei
4. Nuclear reactions where the neutron is absorbed into the nucleus and charged particles are emitted.

Chapter 3

Introduction to Gaseous Detectors

It is quite fascinating how a seemingly-simple process like ionization can lead to a vast range of detector designs, particularly through avalanche processes. The underlying principle in most gaseous detectors in one form or another is electromagnetic interactions. Once an incident ionizing particle enters a gaseous detector, it ionizes and produces one or more primary electrons. External electromagnetic fields present provide kinetic energy to these electrons to accelerate and gain enough energy to create secondary interactions and produce more ion-electron pairs, thus generating a readable output. There are different innovative designs of gaseous detectors to achieve the above characteristics. Before we start describing the evolution of gas detectors since their advent, we will look at features governing the behavior of gas detectors.

3.1 Physical Processes in Gaseous Detectors

3.1.1 Mobility of Charge Carriers

Electrons and ions formed when an ionizing radiation passes through the detector volume gain kinetic energy due to the external electric field present. The velocity of charged carriers depends on the electric field (the average velocity it attains is called the drift velocity) and on the thermal motion. The drift velocity of the ions is given by the following equation:

$$v = \mu \frac{X}{p} \quad (3.1)$$

where v is the drift velocity, μ is called the ion mobility, X is the electric field strength, and p is the pressure of the gas. μ is a factor that depends on the gas used and is inversely proportional to the molecular mass of the gas. Equation 3.1 is valid when (X/p) is small.

A typical value of ion mobility for Argon ions is $1.9 \times 10^3 \text{ Torr.cm}^2/(\text{V.s})$. In this limit, the mobility of electrons is around $10^6 \text{ Torr.cm}^2/(\text{V.s})$, thus meaning that electrons are about 1000 times faster than ions in the gas volume. When (X/p) is large, the drift velocity is given by:

$$v = \text{const} \times \left(\frac{X}{p} \right)^n \quad (3.2)$$

where n lies between 0.5 to 0.8 [2].

3.1.2 Avalanche Multiplication

Let us say a primary electron is created in the gas medium, and λ is the mean free path of the electron for a secondary ionizing collision, then $\alpha = 1/\lambda$ (also known as the first Townsend coefficient) is the probability of an ionization per unit path length (See Appendix A.2 for more details). This coefficient varies for different gases and for n primary electrons, we have:

$$dn = n_0 \alpha dx \implies M = \frac{n}{n_0} = \exp(\alpha x)$$

where M is the multiplication factor, or the gas gain. In the case of non-uniform fields, α is a function of the field, in which case, we have:

$$M = \exp \left(\int_{x_1}^{x_2} \alpha(x) dx \right) \quad (3.3)$$

The dependence of α on the gas pressure and electric field strength is given by [1]:

$$\frac{\alpha}{p} = A \exp \left(\frac{-Bp}{E} \right) \quad (3.4)$$

where p is the pressure, and A and B are parameters depending on the gas used.

3.2 Modes of Operation

To study the modes of operation of a gas detector, let us consider a proportional counter (made from a cylinder of conducting material (cathode) and a thin wire (anode) inside the cylinder. The cylinder is sealed to make it gas-tight with a window. When an ionizing

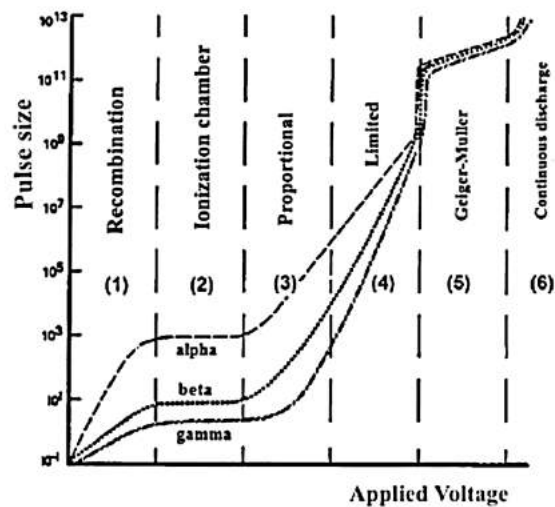


Figure 3.1: Modes of operation of a gas detector. Source: <https://www.intechopen.com/chapters/48796>.

radiation enters the detector volume, there are primary electrons created through ionization, and the energy that these electrons gain is dependent on the external electric field present.

At zero voltage, there is no current collected as the primary electrons recombine with the ions, but as the voltage is slightly increased, electrons are able to overcome the recombination forces and reach the anode. This is known as the recombination region. As one reaches the ionization chamber region, all the primary electrons created reach the anode. But the curve is flat in this region, which is because even with an increase in voltage, the electrons do not gain sufficient energy to ionize further atoms. Secondary ionizations occur after a certain voltage, and this marks the beginning of the proportional region. For voltages in this region, the secondary electrons created also accelerate to produce more ionization and so on. The number of electron-ion pairs in the avalanche is directly proportional to the number of primary electrons. Beyond the proportional region, the charges created distort the electric field leading to a loss of the proportionality. This region is called the region of limited proportionality. For voltages beyond this region (Geiger-Muller region), the energies gained are so high that discharges are produced, and avalanches spread out along the entire anode wire. The last region is known as the continuous discharge region, where the field in the detector is so high that it itself ionizes the gas and produces discharges.

Today we have access to technologies that can help detect the signal output when a gas

detector is operated in the first four regions. Such technology was not present during the time the first gas detector (the GM counter) was invented. When a detector is operated in the GM region, there are discharges upon being incident with radiation, and these discharges can be seen and heard. The fact that we do not need sensitive equipment to operate this device was what led to the invention of the gas detector. One point to note is that this device was operated at low pressure. The drift velocity of ions and electrons is inversely proportional to pressure (as can be seen in Equation 3.1 or 3.2), leading to higher energies at lower pressures.

Development in technology over time gave rise to the possibility of operating gas detectors at lower voltages. In 1968, Georges Charpak invented the Multi-Wire Proportional Counter (MWPC), and this invention marked the beginning of the extensive use of gas detectors in high energy physics experiments. A brief account of the same have been discussed in the following sections along with how they formed a crucial part of the evolution of gas detectors.

3.3 Proportional Counter

A proportional counter consists of a cylinder that acts as the cathode and an anode wire placed inside the cylinder along the axis of the cylinder. The cylinder is filled with a gas mixture, and there is an entry window for the incident radiation to enter the detector volume.

When a positive voltage is supplied to the anode wire, the electric field inside the detector volume can be calculated using the Laplace equation and the continuity of the electric field. Let us say a and b are the radii of the anode wire and outer cylinder, respectively. Then for a point r distance away from the axis of the wire ($a \leq r \leq b$), we have:

$$V(r) - V(a) = -\frac{\lambda}{2\pi\epsilon_0} \ln\left(\frac{r}{a}\right)$$

where λ is the charge density of the wire, and $V(a)$ is the voltage applied to the anode wire. Using the boundary condition we have (voltage at the surface of the outer cylinder), we get:

$$V(b) - V(a) = -\frac{\lambda}{2\pi\epsilon_0} \ln\left(\frac{b}{a}\right) \implies \lambda = -\frac{2\pi\epsilon_0}{\ln(\frac{b}{a})}(V(b) - V(a))$$

After using the above two equations, setting $V(b) = 0$ (we ground the outer cylinder in the

proportional counter), and using $E(r) = \lambda/2\pi\epsilon_0 r$, we get:

$$E(r) = \frac{V(a)}{r \ln(\frac{b}{a})} \quad (3.5)$$

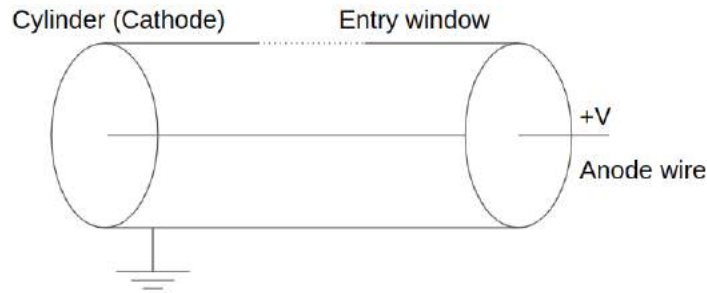


Figure 3.2: Schematic diagram of a proportional counter.

To show how high electric fields are achieved in a proportional counter, let us take an example of a cylinder of radius 1 cm and an anode wire of radius 0.01 cm. If a voltage of 2000 V is supplied to the anode wire, equation 3.5 tells us that at a distance of 0.011 cm from the center, an electric field of around 40 kV/cm is achieved. Higher electric fields for distances closer to the anode wire.

When an ionizing radiation enters the detector volume, there are electron-ion pairs generated in the gas volume. Due to the electric field, the ions drift towards the cylinder, and the electrons drift towards the anode wire. As electrons drift towards the wire, the magnitude of the electric field increases, and they achieve sufficient energy to ionize further atoms. This initiates an avalanche effect, thus inducing a readable current in the anode wire. The signal induced consists of a sharp rise and a long tail. There are two factors that give rise to such a signal. The drift velocity of electrons is much higher than that of ions, so the signal induced from electrons rises and falls fast, but since the ions are drifting towards the cylinder slowly, they contribute to a long tail in the signal. Secondly, most of the electrons and ions are formed close to the anode wire, so the electrons travel a short distance to reach the wire as compared to the ions needing to travel almost the length of the radius of the cylinder (which is usually in the order of centimeters).

3.4 Multi-Wire Proportional Counter

The MWPC is what one would obtain if multiple proportional chambers were duplicated and combined. It consists of a set of thin, parallel, and equally spaced anode wires between two cathode planes. Negative potentials are applied to the cathode, and the anode is grounded. Once an incident ionizing particle ionizes the gas molecules as it traverses through the detector, electron-ion pairs are generated, and they start drifting towards the electrode. The electric fields present in this setup are sufficient to provide enough energy to ionize further electrons and thus generate a readable signal. The cross-sectional schematic diagram of the MWPC is shown in Figure 3.3.

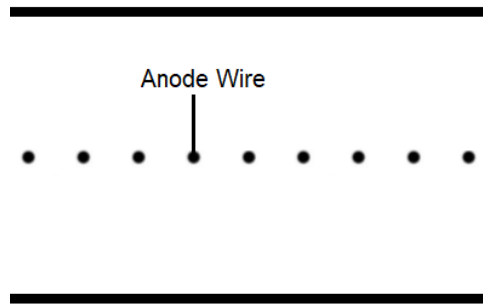


Figure 3.3: A cross-sectional schematic diagram of an MWPC.

The MWPC has a good spatial and energy resolution, but issues persisted with the rate capability, and owing to the slow evacuation of positive ions, a buildup modified the electric fields. Nevertheless, the MWPC gave rise to the advent of detectors based on unique ideas like the drift chamber. Then the drift chamber and the MWPC coalesced to form the Time Projection Chamber.

3.5 Micro-Strip Gaseous Chamber

Despite the success of the MWPC, there was a need to improve upon the MWPC's capabilities and the advances in photo-lithography techniques and microelectronics helped with the creation of the Micro-Strip Gaseous Chambers (MSGCs). MSGCs can achieve rate capabilities of around 10^6 counts $\text{mm}^{-2}\text{s}^{-1}$ when compared to 10^4 counts $\text{mm}^{-2}\text{s}^{-1}$ in MWPCs [3]. The MSGC consists of alternately placed narrow and wide thin metallic strips

placed on an insulator. There is also a drift cathode plate on top. The narrow and wide strips are anodes and cathodes, respectively, and the electric fields around these strips can increase to orders of kV/cm. As mentioned in Ref. [3], and [4], the form of the electric field is such that the ions produced by the avalanche evacuate rapidly, thus crossing the hurdle MWPCs could not by providing better rate capabilities.

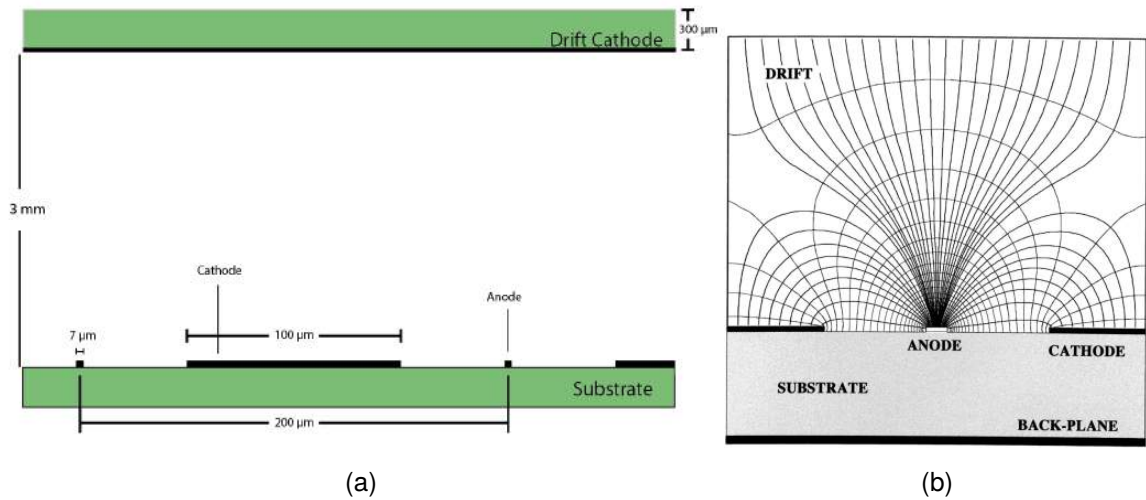


Figure 3.4: (a) A schematic cross-sectional diagram of the MSGC with typical dimensions. (b) The electric field lines of the MSGC. Source: [5]

One particular disadvantage of MSGCs is charging up effects (in the insulating surface at the bottom). This arises due to the diffusion of electrons and ions generated during the avalanches. The charges accumulated can result in discharges that can melt the metallic strips. In a later section, we will see how the Thick-GEM detector is a more robust detector with respect to these kinds of issues than most gaseous detectors.

Following Oed's path came a class of detectors known as the Micro Pattern Gaseous Detectors (MPGDs), of which, the GEMs and Thick-GEMs are a part of.

3.6 Micro Mesh Gaseous Detector

The MICRO MESH GASEOUS (micromegas) detector has a metallic micro-mesh that divides its gas volume into two parts. However, the multiplication region (the region below the mesh, about 50-100 μm in height) is very narrow compared to the region above the mesh. There is a drift electrode on top and readout strips on the bottom. The amplification

happens around and under the mesh. High electric fields (40–80 kV/cm) are created in the amplification gap by applying a voltage between the grid and the anode [4].

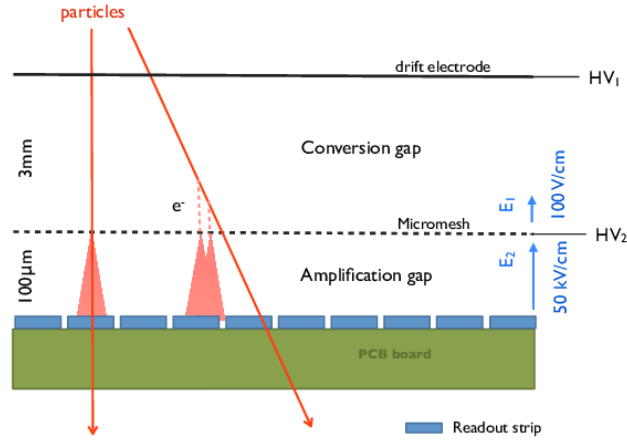


Figure 3.5: Schematic diagram of the micromegas detector. Source: <https://iopscience.iop.org/article/10.1088/1748-0221/7/03/C03040>.

As explained in [3], these detectors offer good spatial resolution and have a fast response owing to the small amplification gap, where the large number of electrons produced have to travel for a small distance to reach the readout.

3.7 Gas Electron Multipliers

In 1996, Fabio Sauli introduced GEMs [6], which are electron multipliers made from a copper-cladded polymer foil perforated by a high density of holes. The GEM electrode contains a geometric pattern of hourglass-shaped holes and is produced by certain etching techniques. High voltages are applied on both copper surfaces to provide for a high voltage gradient. The hole shape of the foil is such that there is a dipole-like field (See Figure 3.6b) that can help with a focused electron path at the center and high gains through multiplication because of the high field values in the hole.

The GEM detector is similar in design to the previous detectors. There is a drift electrode above and readout strips underneath the GEM foil, respectively. The typical dimensions and specifications of the detector will be discussed soon.

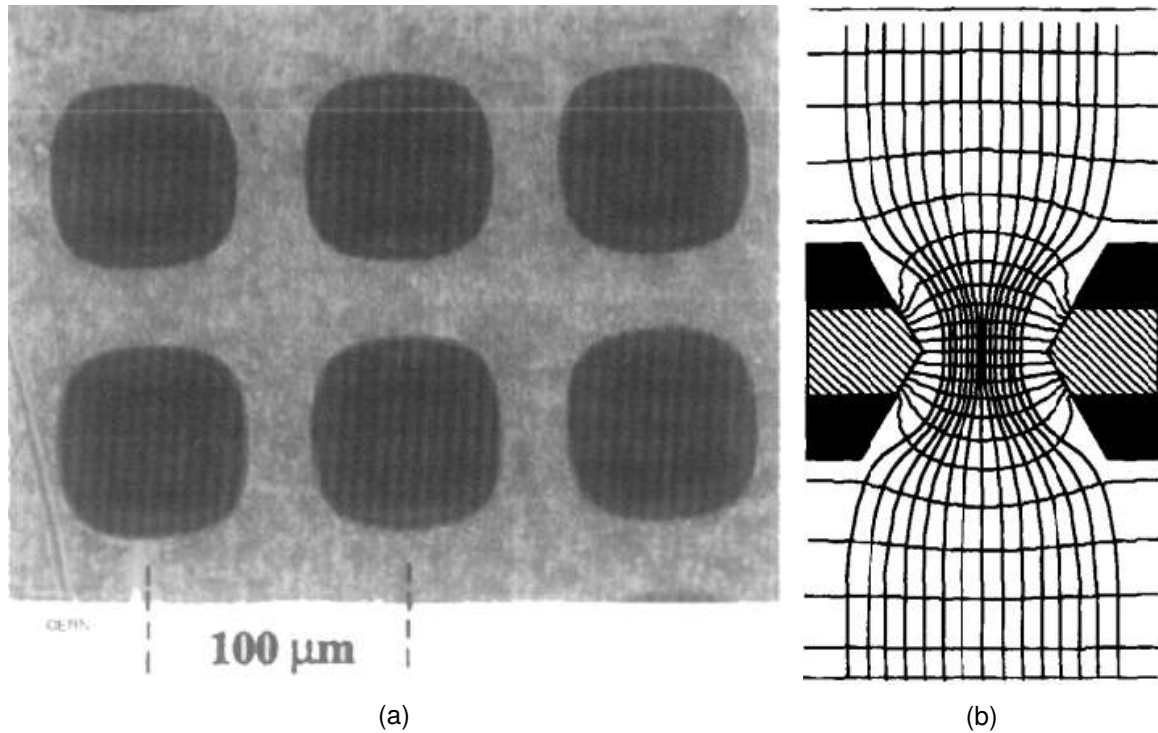


Figure 3.6: (a) A top view image of the GEM foil. (b) The electric field lines across a GEM hole. Source: [6]

When an ionizing particle passes through, it produces primary charges by ionization. Through drift and diffusion processes, the charges are transported through the gas volume to the amplification region close to the electrodes. These charges will attain high velocities due to the high electric field and cause further ionizations leading to an avalanche effect. This avalanche process is also called the Townsend avalanche and is studied in great detail in Ref. [5]. The first Townsend coefficient is a variable that has been extensively studied in gaseous detector physics and represents the number of ion pairs produced per unit length of drift [5]. These charges are then collected by the readout pads under the GEM electrode. Separated from the multiplying electrode, the charge collection and readout plane can be patterned at will with strips or pads; usually, they are a set of perpendicular strips to serve as a 2-dimensional readout.

As explained in [5], the GEM detector, with cascaded GEM foils, can reach very high gains without getting destroyed. This is an important point as previous detectors like the MSGCs involved damages when attempts to reach higher gains were made. The readout

also can be patterned depending on the user's needs.

3.8 Thick-Gaseous Electron Multipliers

The Thick-GEM detector is a variant of the GEM detector with dimensions blown up by a factor, with changes in some structural aspects. Thick-GEMs have a cylindrical hole shape compared to an hourglass shape in GEMs, which also means the etching process to make these holes is different. Keeping in mind the difficulty in making a precision device such as a GEM foil with its very fine hole diameter along with its small pitch, the Thick-GEM came out to be a device cheaper and easier to manufacture. The GEM foil needs high-precision tools to make structures at such dimensions (and its holes are made through a chemical etching process), but the Thick-GEM can be made without such stringent requirements (the holes in a Thick-GEM foil are drilled mechanically). Figure 3.7 and Table 3.1 gives us a better idea of the difference between both detectors in terms of foil specifications. Furthermore, Thick-GEM detector is also very “robust”, which means that it has good strength against mechanical force, high electrical fields, ease of handling, etc. As mentioned before, other detectors like the MSGCs can get destroyed while operating at high fields; typical GEM electrodes are also sensitive to sparking and can be permanently damaged after a significant discharge. However, the etched rim in a Thick-GEM helps reduce edge discharges [7].

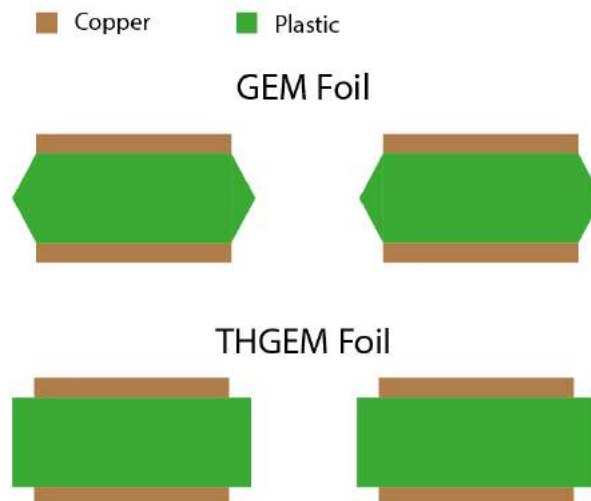


Figure 3.7: Cross-section schematic of the GEM and Thick-GEM holes (Not to scale).

Table 3.1: Comparison of some specifications between a typical GEM and Thick-GEM foil.

Measurement	GEM	Thick-GEM
Hole Diameter (Inner)	50 μm	0.4 mm
Hole Diameter (Outer)	70 μm	0.6 mm
Pitch	150 μm	1 mm
Thickness	60 μm	0.5 mm
Electric Field	30-80 kV/cm	15-25 kV/cm

Chapter 4

Development of the Thick-GEM Detector

4.1 Overview

This Chapter will deal with the intricate details of the work done to fabricate and assemble the Thick-GEM detector and discuss the results obtained from a few simulations that were performed using Garfield++ [8]. The main paper that was referred to for guidance is Ref. [9]. It is to be noted here that the fabrication process was a continuation of the work done by me during a previous project. In particular, everything described after Sections 4.2 and 4.3 in this Chapter was done as part of this Master's Thesis.

The detector comprises three main elements: the drift electrode, the Thick-GEM foil, and the readout pads; all of them are placed inside a gas enclosure, with a window on top that is transparent to incoming particles but yet keeps the detector gas-tight. The drift electrode is usually a metallic mesh with a voltage to provide a drift field, usually of magnitude 2 kV/cm. As the name explains, the drift electrode makes the charges produced under it attain a drift velocity, so they are directed towards the Thick-GEM electrode. The electric field produced in the Thick-GEM holes due to the voltage supplied on both copper surfaces is usually around 30 kV/cm. Under the Thick-GEM electrode is the induction gap with an electric field, usually around 1 kV/cm. This region helps in directing the electrons to the readout pads where the signal-current is generated, thus giving us a readable output. The entire setup will be in a gas-tight gas enclosure made with perspex on the sides, Mylar as the top layer (also serving as a window for incoming particles), and the bottom will be a PCB board with readout pads. The detector can be divided into three regions based on the electric field values that will be applied, namely the drift region, Thick-GEM hole region, and the induction region. The same has been labeled in the schematic diagram shown in Figure 4.1. The Thick-GEM foil we are using is 0.25 mm thick, and inner and outer hole diameters of 0.2 mm and 0.3 mm, respectively. The pitch between the holes is 0.45 mm.

The following components are needed to construct the detector fully:

- Outer gas-tight enclosure and top-enclosure
- Readout strips
- Drift electrode
- Electronics

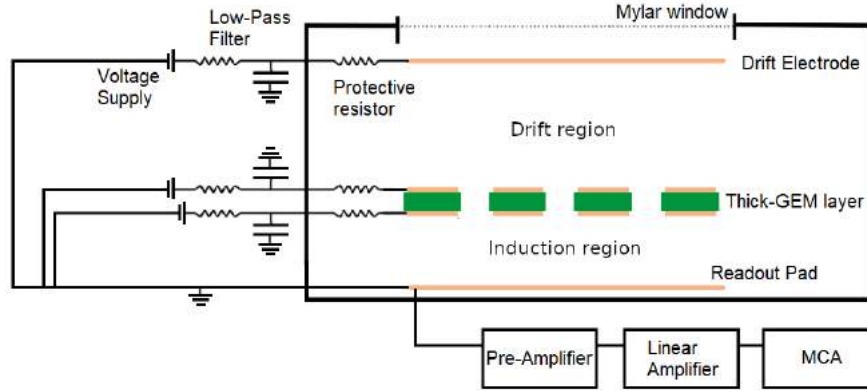


Figure 4.1: A cross-sectional schematic diagram of the detector and the electronic circuits used.

The subsequent sections will describe the components and provide details of the manufacturing process, if relevant.

The drift electrode is essentially Aluminum tape pasted on a Mylar sheet (with a contact for a connection to the voltage source). The sheet is held by a Poly-Lactic Acid (PLA) frame (3D printed) to provide support and keep it flat, so it does not bend due to its weight. The dimensions of the working area of the drift electrode is $10 \times 10 \text{ cm}^2$. Under the drift electrode is the Thick-GEM foil which has three layers, a top copper electrode, a middle FR4 layer, and a bottom copper electrode. The total working area of the Thick-GEM foil is also $10 \times 10 \text{ cm}^2$. The Thick-GEM foil was procured from Micropack Pvt. Ltd., Bangalore, which is the only component we outsourced for our detector. The anode then comes under the Thick-GEM foil, which in our case are the readout strips. The Thick-GEM foil and the drift electrode are kept at a height of 2.5 mm and 7.5 mm from the base, respectively, using nuts. There is thus a gap of 5 mm between the drift electrode and the Thick-GEM foil. Figure 4.1 is a schematic diagram explaining the same.

Rectangular copper strips are provided at the drift electrode and Thick-GEM foil for the voltage connection (See Figure 4.2). The contacts from different layers of the electrode

have been connected to other contacts for extension purposes, which will come out of the gas enclosure and can be understood by looking at Figure 4.3. This makes applying the required voltages to each layer outside the gas-tight chamber easier.

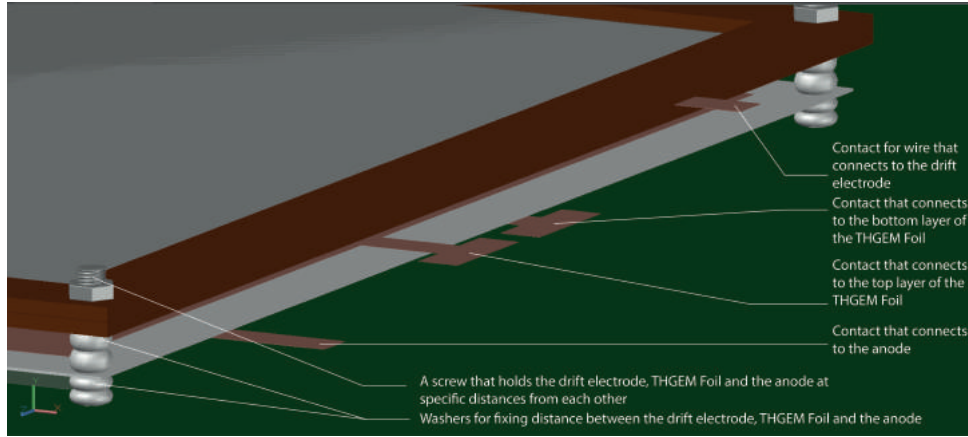


Figure 4.2: Isometric view of the design of the detector made using AutoCAD.

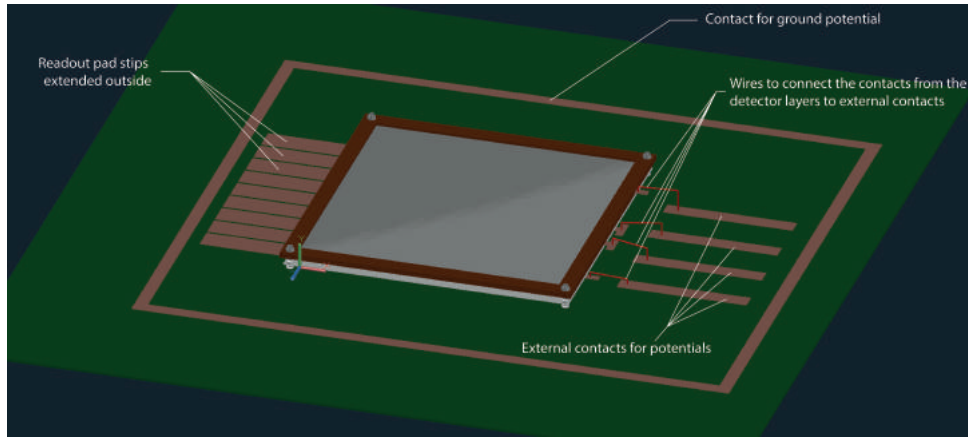


Figure 4.3: Second isometric view of the detector.

We finally close everything with an enclosure of height of 1.5 cm, which will make the entire setup gas-tight, and we also provide an inlet and an outlet valve for gas flow (See Figure 4.4). The top portion of the enclosure is made of PLA and a Mylar window (which would serve as a window for incoming particles). Perspex is used for the sidewalls of the enclosure.

The contacts for the four potentials for the detector will all be connected to a serial 10 M Ω resistor, a 50 Hz low pass filter (using a 2.2 nF capacitor and a 10 M Ω resistor), and

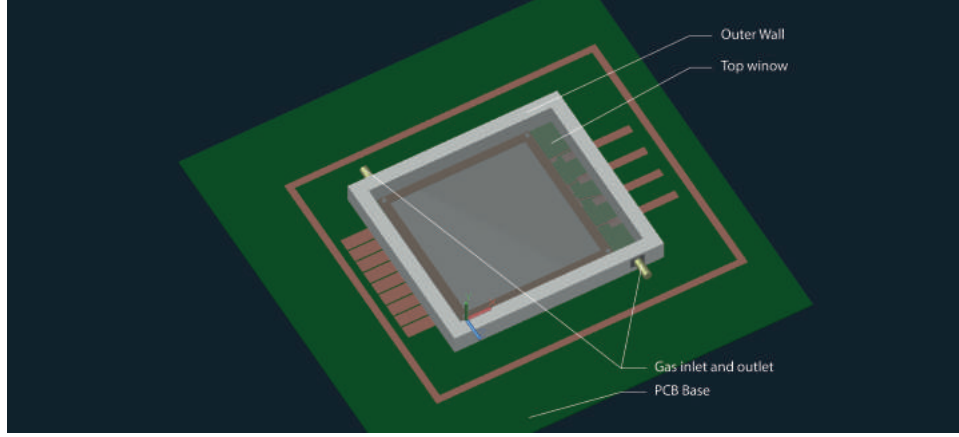


Figure 4.4: Top view of the detector showing the two electrodes and the Thick-GEM Foil.

then to the power supply, which is a CAEN N1470 High Voltage (HV) supply. The series resistance is added as a protective resistor (against current surges), and the low pass filter is to limit AC voltages that can arise from the voltage supply. We will see that frequencies in voltages can act as a source of noise in a later section. The potential that will be supplied to the contacts is shown in Table 4.2.

Surface	Potential (V)
Drift Electrode	-2000
Top layer of Thick-GEM foil	-1500
Bottom layer of Thick-GEM foil	-500
Anode	Gnd

Table 4.1: Typical potentials that are supplied to each electrode in the detector.

For the potential values applied, the electric field magnitudes for different regions would correspond to the values shown in Table 4.2. These were also the same field values used in Ref. [9]. But there are no universally fixed field values for these regions. They vary based on the detector specifications and other aspects like materials used, quality of assembly, etc.

Region	Height (mm)	Field (kV/cm)
Drift region	5	1
Thick-GEM hole region	0.25	40
Induction region	2.5	2

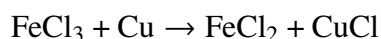
Table 4.2: Dimensions and electric field magnitudes for different regions in the detector

The readout strips were connected to the preamplifier, a linear amplifier (CAEN Spectroscopy Amplifier M968), a Multi-Channel Analyser (MCA) (Ortec 927 ASPEC MCA), and finally, a computer to store the output from the MCA.

4.2 PCB and Readout Strips

Ten readout strips made of conducting material (Copper in our case) were required to be placed under the Thick-GEM electrode. So a Printed Circuit Board (PCB) board with copper-clad on both sides was taken as the base from which Copper will be etched out, leaving only the readout strips behind.

In order to etch out the unwanted copper, we carried out a displacement reaction using a FeCl_3 solution. The corresponding displacement reaction is as follows:



We prepared a mask using readily available toner ink, which acted as a physical barrier, under whose region the FeCl_3 would not react. So after dipping the board in this solution FeCl_3 would remove copper wherever the mask was not present. Using a laserjet printer, we printed the mask layout on OHP sheets (these are transparent sheets used for Over-Head Printers, from where the name arises). These sheets were then placed at appropriate positions on the PCB board and ironed, due to which the toner ink on the sheets was transferred to the PCB board, thus completing the masking process. Then an appropriate FeCl_3 solution was prepared, and the board was placed in the solution and was agitated until all the copper from the desired regions was removed. We washed the toner ink with Propanol to remove the mask, which removed the ink but not the Copper under it. An image of the board after this etching process is shown in Figure 4.5.

4.3 Drift Electrode

The drift electrode was made with Aluminum, Mylar, and a frame to hold the Mylar and Aluminum flat and sturdily. The support structure frame is made of PLA and was designed and 3D printed (printed using NISER's Robotics Club's 3D printer). Then a Mylar sheet was stuck on top of the frame to serve as a base for the Aluminum tape to be pasted upon. The

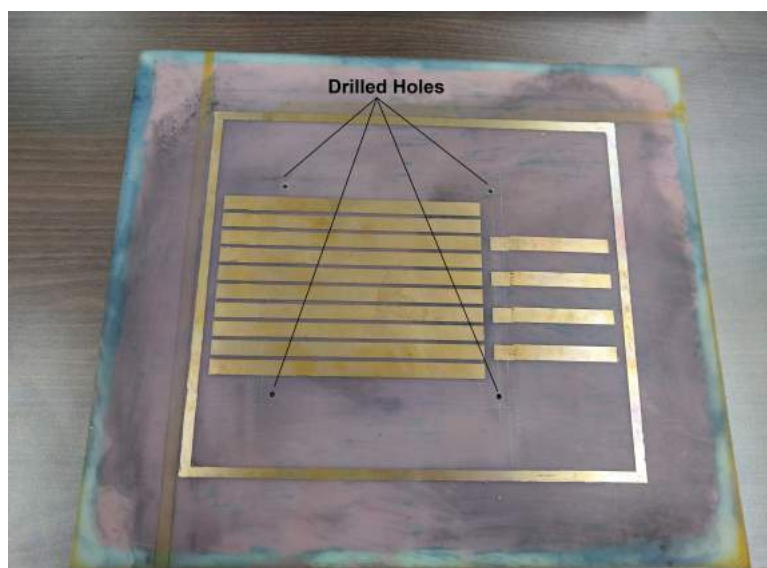
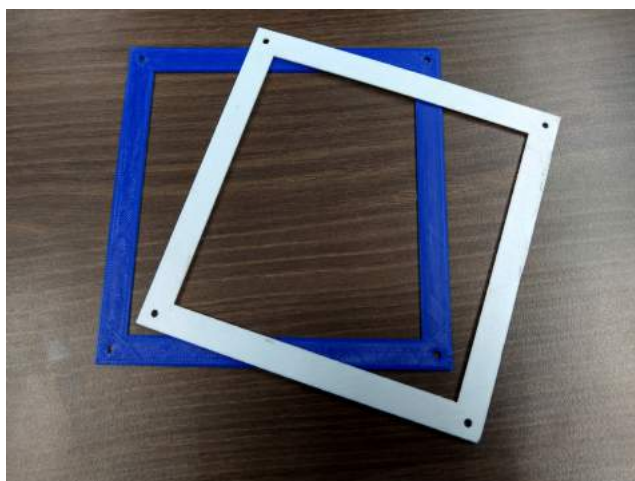
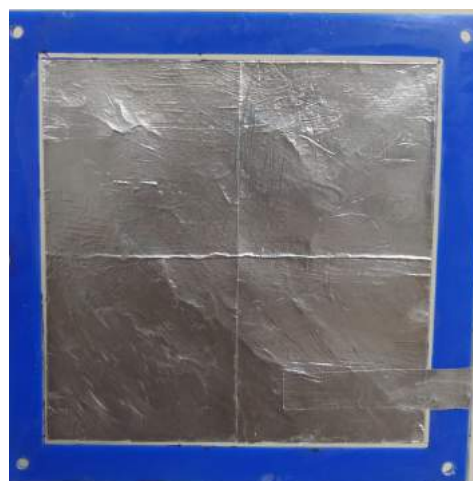


Figure 4.5: The PCB with the readout strips and other terminals after the chemical etching process. Four holes were also drilled, which will be used to hold the Thick-GEM foil and the drift electrode.

voltage supply would be connected to this Aluminum layer with the voltage as mentioned in Table 4.1.



(a)



(b)

Figure 4.6: (a) The frame of the drift electrode and (b) an image of the fully-constructed drift electrode.

4.4 Gas-Tight Enclosure

The Thick-GEM detector has an inlet and an outlet for gas flow, and the remaining volume needs to be gas-tight. To form a gas-tight container around the anode, foil, and drift electrode, we made four walls using Perspex along with an inlet, and an outlet for the gas flow (See Figure 4.7a), with a top enclosure. The interior dimensions were approximately $15.4 \times 14.4 \times 1.5 \text{ cm}^3$. The top enclosure was made with a 3D printed structure with an open window that was covered with Mylar which would serve as an entry for incident radiation.¹ The objective was to make a top enclosure that could be opened and sealed if we needed to change components or perform some checks. All components inside this chamber would be in a gas-tight environment, with gas being brought in and flushed out at a constant rate.

Since the side walls were sealed with Araldite, they are never tampered with and do not account for any gas leak. The Mylar sheet that would be placed for the window was pasted and sealed with Araldite. The only source for a gas leak can arise from the top enclosure, and motivated by the design of O-ring joints [11] (See Figure 4.8a) that are used in vacuum chambers, we designed an enclosure that, when tightened to the Perspex frame with screws, can form a gas-tight joint. We experimented with many designs, but the final top enclosure has a protruding ridge from the flat surface (See Figures 4.7c, 4.8c). The entire wall was drilled with holes so that screws can go all the way and be able to lock the top enclosure to the Perspex walls. For a good seal, we cut a rubber mat and placed it on top of the Perspex later (See Figure 4.7b). Gas leak tests were also conducted with different materials like thermoplastic elastomers², foam, Teflon layers, etc.

We performed a gas leak test, i.e., measured the rate at which gas leaks for different pressures for the design that was finalized. We flow some gas inside the detector and then block the inlet and outlet valves, leaving the detector with gas inside it at some initial pressure. We then note the pressure inside it (using a U-tube manometer) at certain intervals of time. The initial designs had performed very badly, losing all gas in a matter of seconds. The manometer does not provide us with information about where the leak is occurring. We then gauged the amount of gas leaking and regions from where it is leaking by placing the

¹Although can be included in a future test, we do not know if PLA would allow particles of our source (5.9 keV X-Rays from ^{55}Fe) to pass through, whereas Mylar and Kapton are materials used as a window for irradiated particles to pass through [10].

²a material that increases in tack when heat is applied; such materials used in glue-guns

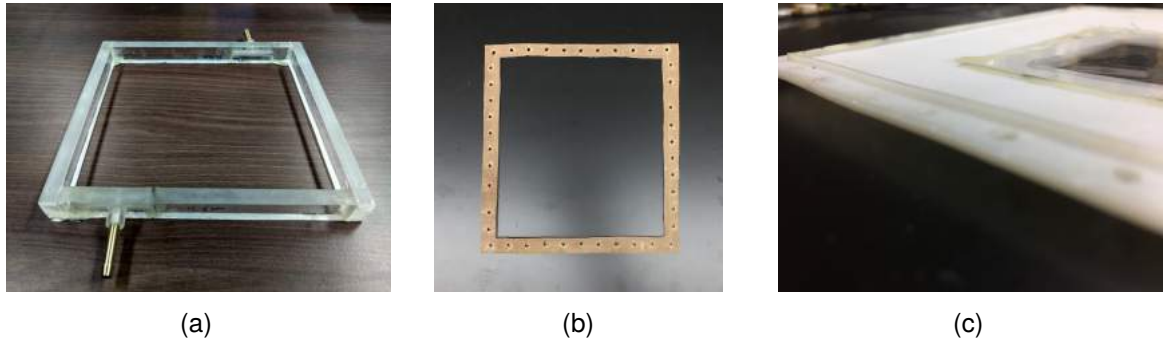


Figure 4.7: (a) The Perspex frame with the inlet and outlet valves. (b) The rubber layer that will be placed on top of the Perspex layer to act as a seal for the joint. (c) A zoomed-in image of the top enclosure to show the ridge.

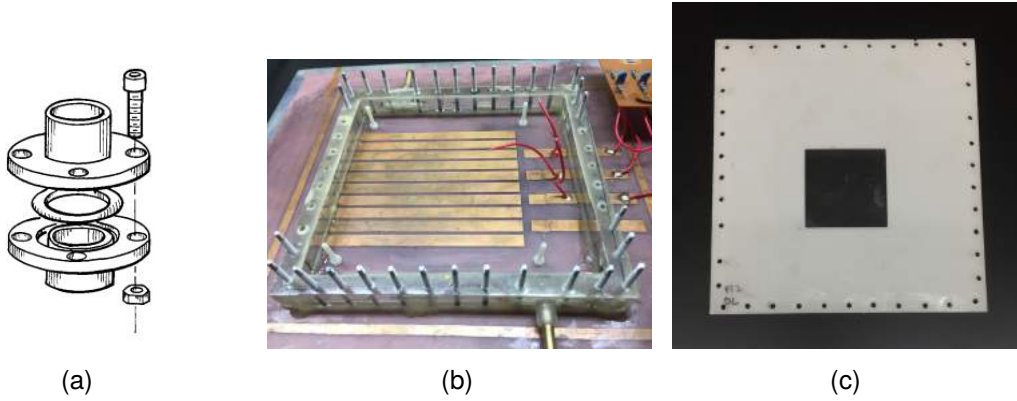
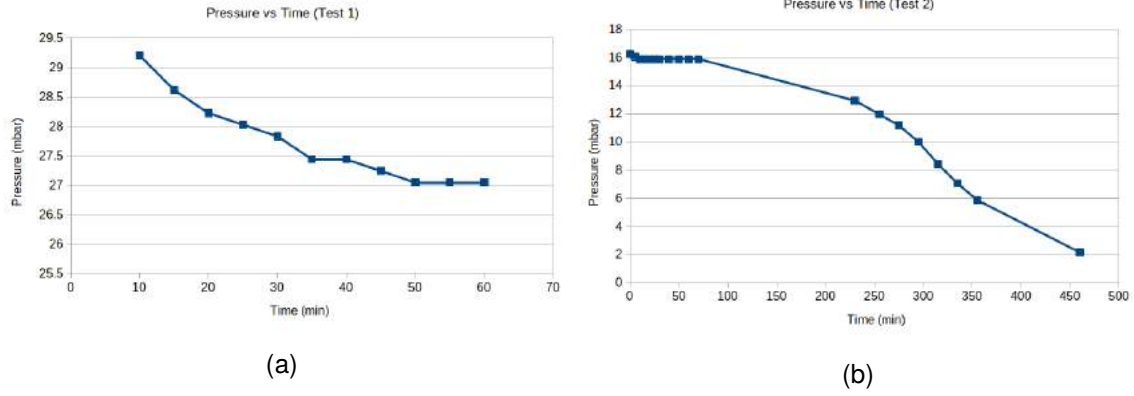


Figure 4.8: (a) An O-ring sealed vacuum connection (Source: [11]). (b) An image of the detector after the placement of the Perspex walls and installation of screws taped with Teflon to prevent gas leaks. (c) Image of the top enclosure.

setup (without the foil, drift electrode, and electronics, but with the gas flow) underwater. This gave rise to bubbles from locations where the setup has gaps or holes. When we arrived at a setup where there were no bubbles visible, the pressure drop (measured with the manometer) was still not satisfactory. Dipping the setup in soap water instead of water further provided us with additional areas of improvement that were needed to make the setup leak-proof. After these changes, the plot of pressure inside the container vs. time was plotted and is shown in Figure 4.9b, but after tightening the screws of the joint between the Perspex frame and top enclosure, the subsequent gas leak test (See Figure 4.9b) which was performed for a larger period) gave a lesser leak rate.

Based on a couple of gas-leak tests, we were able to obtain an average leak rate of about



change the supply points.

An Ar+CO₂ (70%-30% ratio respectively) was used as the gas mixture, and the setup was flushed with this gas mixture for a few days until the detector was tested.

4.6 Gas Selection and Quenching Gases

The Thick-GEM detector is a gaseous detector, but we never discussed what gases to use or why to use them. For the selection of the gas mixture, one needs to keep in mind that the gaseous constituents should not have a high electron affinity to attract the electron before it even begins the avalanche effect. Keeping in mind the physical conditions required to keep the substance in its gaseous state, noble gases are good choices. After ejecting an electron, one might argue that the noble gas atom attains halogen configuration, but by the time it pulls the electron, the electron under the external electric field would have begun subsequent collisions. There are other favorable reasons for noble gases. Nobles gases are inert, and that is also why they are a good choice, and what is meant by this is that they are chemically inert, so they do not react with the detector materials. They also do not catch fire easily, and this is relevant because sparking is something very likely to happen in such detectors. We do not need gases that catch fire inside during the experiment.

We also add other relatively inert gases like CO₂ and CH₄ to the gas, and they are called quenching gas. This is done to reduce the gain, as a very high gain can also lead to a higher discharge probability. Higher discharge probability means higher chances for the Thick-GEM foil to get destroyed. These gases are electronegative, so at times they absorb the electron from an ionized atom preventing further amplification.

4.7 Electronics Used

The protective circuits for the HV supply were mentioned before. Additionally, we have the equipment to obtain, shape, and amplify the signal from the readout strips. This section describes the various components and the subsequent electronic circuits/connections. The train of electronics from the readout strips is the preamplifier, amplifier, and MCA.

4.7.1 Preamplifier

The readout strips are first connected to the preamplifier, and we used an Ortec 142 IH charge-sensitive preamplifier (or preamp) [12]. The primary function of a preamplifier is to extract the signal (which in our case, are charges that originate due to primary and secondary ionizations) without degrading the signal-to-noise ratio. This is usually why the preamplifier is placed close to the detector, so that the characteristics of the signal are not disrupted by factors like capacitance changes by cabling, radio-frequency pickup, etc. A charge-sensitive preamplifier is generally used for energy spectroscopy, and these preamplifiers can measure the quantity of charge and time of arrival. A preamplifier would consist of an operational amplifier with a feedback capacitor, which acts as a charge integration circuit, thus converting the number of charges to a voltage value. The amplitude of the output is proportional to the quantity of charge.

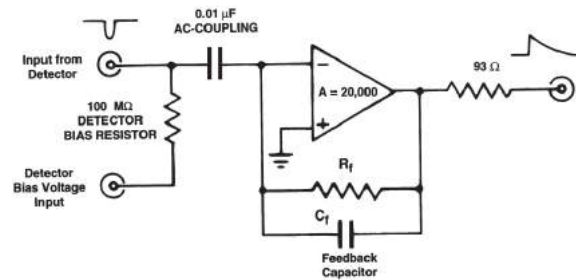


Figure 4.10: A circuit diagram of a typical charge-sensitive preamplifier. This figure shows how a typical input pulse and output look like. Source: [12]

4.7.2 Spectroscopic Amplifier

The CAEN N968 Spectroscopy Amplifier [13] that was used in the experiment has a variety of functions like amplification, shaping, pile-up rejection, pole-zero cancellation, and baseline restoration. The output of the preamplifier will be connected to the spectroscopy amplifier for further pulse processing.

The shaping is done through a CR-RC-shaping circuit, and for pedagogical reasons, we describe a simple CR-RC-shaping circuit.

The output of the shaping circuit looks like the output of the amplifier, as shown in Figure 4.11. Additional shaping can be done by varying the time constants of the RC/CR

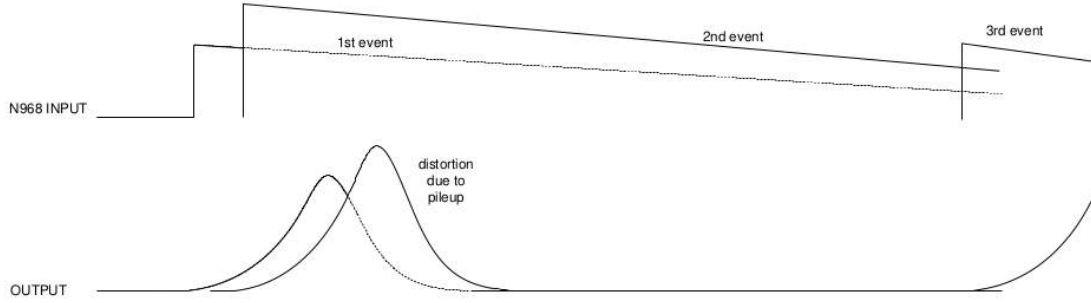


Figure 4.11: A schematic diagram of the input pulse to the amplifier and the output pulse. The inter. We see that the output pulse has been shaped, which is done through a shaping circuit. Source: [13]

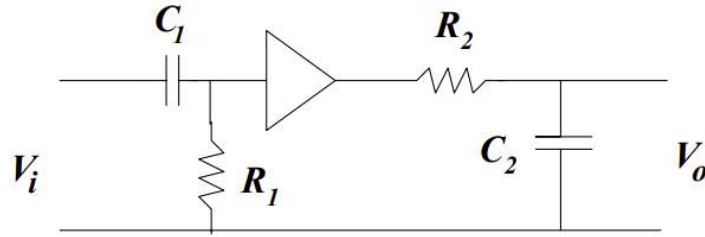


Figure 4.12: The schematic diagram of a typical shaping circuit. Source: [14]

circuits. Figure 4.13 conveys the same.

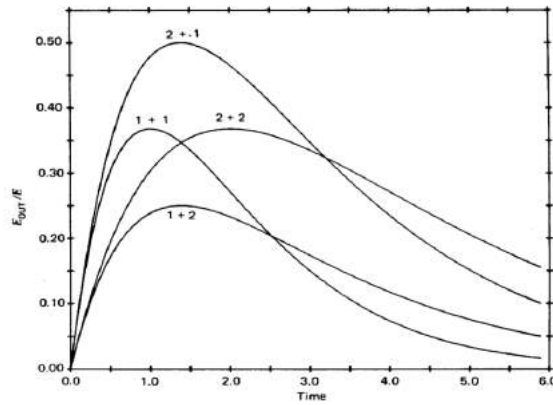


Figure 4.13: The outputs of a CR-RC shaping circuit to a step voltage. Curves are shown for several different combinations of time constants and are labeled as (time constant of CR circuit + time constant of RC circuit). Source: [14]

4.7.3 Multi-Channel Analyser

The MCA is the final piece of equipment we use to process the signal before the information is sent to a computer. The MCA is a device that takes in the shaped and amplified pulse from the amplifier and digitizes it, which means it converts analog information to digital information. We used an Ortec 927 ASPEC MCA for the experiment.

4.8 Preliminary Tests

Before we place a source and start performing any experiments, we need to test for any electrical discharges while increasing the voltage supply slowly. The CAEN HV supply has an inbuilt device to measure the current flowing through the circuit, and the least count can go up to $0.05 \mu\text{A}$. To prevent the foil from getting damaged by sparks, we set a limit of $20 \mu\text{A}$ on the CAEN HV module, and if a current greater than this value flows (which can arise if there are electrical discharges), the supply automatically switches off. These tests were carried out in two stages:

1. We first increase only the voltages on the Thick-GEM layers in steps of 20 V until we reach -1500 V and -1000 V for the upper and lower layer of the Thick-GEM foil, respectively. We observed no current greater than $0.30 \mu\text{A}$.
2. We then increase the voltages on the Thick-GEM layers and the drift electrode until we reach -2000 V, -1500 V, and -1000 V for the drift, upper Thick-GEM layer, and lower Thick-GEM layer, respectively. We observed no current greater than $0.30 \mu\text{A}$.

4.9 Measuring the Energy Spectrum of ^{55}Fe Source

Once the required components and circuits that are needed to start taking data are in place, we connected the detector output to the preamplifier input and the output of the preamplifier to an oscilloscope (Teledyne Wavesurfer 510) to see if we get an output close to the expected form (a typical output of a signal from the preamplifier contains a very short rise time and a long decay tail, as shown in Figure 4.10). This setup was used for the rest of the experiments mentioned in this Chapter, unless mentioned otherwise. We then placed

an Iron (^{55}Fe) source ⁴ that produces X-Rays of energy 5.9 keV, to which we observed no signal. We also got no desired output for a Strontium (^{90}Sr) source, which is a β source, thus eliminating concerns regarding the activity of the ^{55}Fe source that was used.

4.10 Components Check

Given that there are no issues from the leak-proof setup and the source, we performed ablative tests with the help of a pulse generator from Agilent (81110A) to see if any of the electronic components we were using was faulty:

1. The oscilloscope was not found to be faulty after the same square wave pulse that was generated from the pulse generator was seen on the oscilloscope too.
2. The preamplifier has an additional connection called the test input, where one can provide a test pulse for calibration and this connection can also be used for testing/additional calculations. But according to [12], the test pulse that goes into the test input connection should have a rise time of around 20-40ns and a decay time of 200-400 μs . The same was achieved using an RC-shaping circuit and appropriate characteristics of a square wave from the test pulse generator. The results of this test indicated that the preamplifier has no faults. See Figures 4.14, 4.15 and 4.15.
3. With the same circuit and settings as above, we connected the oscilloscope to the spectroscopy amplifier, which was connected to the preamplifier. The output on the oscilloscope from the amplifier was Gaussian-like which implies that the spectroscopy amplifier too is working as expected.

Now that the electronic components were found to have no faults, we cornered the problem to the detector or noise ⁵, or both. The pursuit from here is to reduce noise levels or increase the effective gain of the detector.

⁴The ^{55}Fe source produces X-Rays of energy 5.9 keV. This characteristic X-Ray arises because ^{55}Fe converts to ^{55}Mn through electron capture, which in turn leads to a re-arrangement of electrons giving rise to these X-Rays.

⁵Noise can be a reason for not observing the expected output from the preamplifier because there is a possibility that the amplitude of the signal is lesser than that of noise

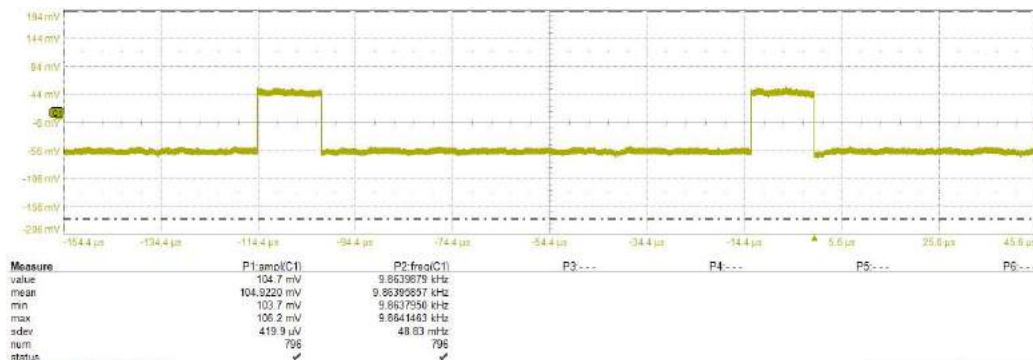


Figure 4.14: The square pulse generated by the pulse generator.

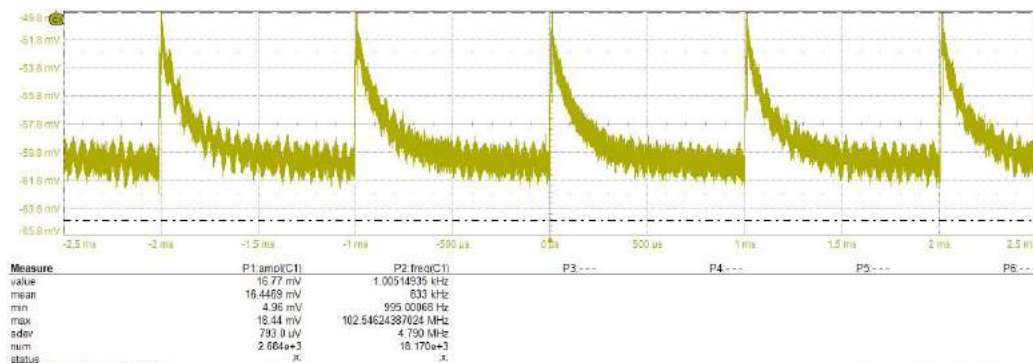


Figure 4.15: The square pulse after being shaped by the RC-shaping circuit.

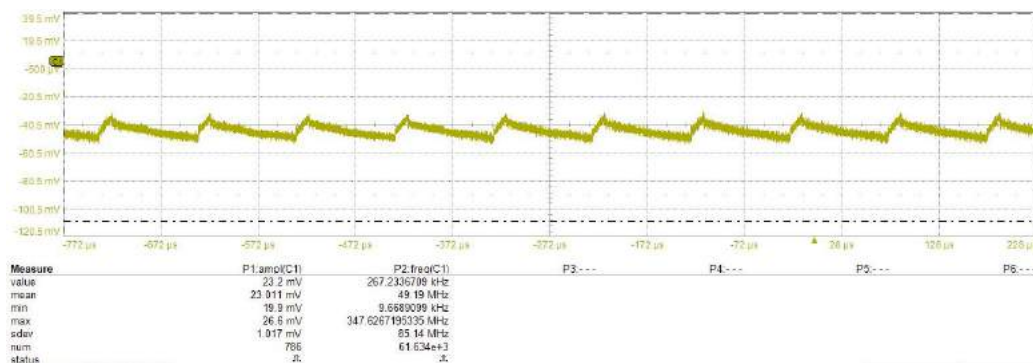


Figure 4.16: The preamplifier output for the input pulse shown in Figure 4.15.

4.11 Study on the Expected Output

With a rough calculation, we can find out the expected output of the signals when measured from the preamplifier. This would give us an idea of how much noise we should reduce or

by what factor the signal should be amplified.

We connected the pulse generator to the test input of the preamplifier and observed the output of the preamplifier on an oscilloscope. For a square wave pulse of height 50 mV, width 60 μ s, and frequency 500 μ s, a preamplifier output with pulses of around the same amplitude was obtained. The feedback capacitor in the preamplifier is what governs the height of the output pulse, and the voltage is given by Q/C_f , where C_f is the capacitance of the feedback capacitor. So we have the following information:

$$50 \text{ mV} = \frac{Q}{1 \text{ pF}} \implies Q = 50 \text{ fC}$$

This means that an input charge pulse of 50 fC to the preamplifier would give us an output of height 50 mV.

We now try and calculate the number of expected charges from the detector after amplification for Argon-CO₂ (70%-30%) mixture and 30 kV/cm field in the Thick-GEM hole region. The ⁵⁵Fe source produces X-Rays of energy 5.9 keV, and the mean ionization energy values (W) for Argon and CO₂ are 25 eV and 34 eV, respectively. The average number of primary electrons produced by an X-Ray is $5.9 \text{ keV} \times \left(\frac{\%(\text{Ar})}{W(\text{Ar})} + \frac{\%(\text{CO}_2)}{W(\text{CO}_2)} \right) = 207.7$ [15]. A more rigorous calculation can be found in Ref. [4].

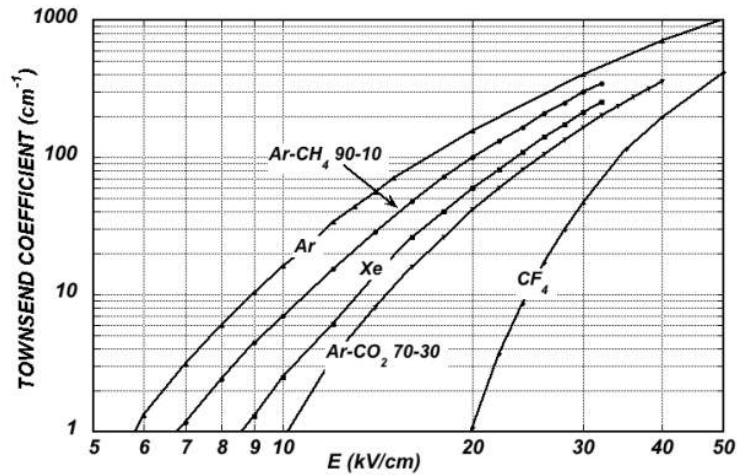


Figure 4.17: Computed first Townsend coefficient as a function of the electric field in several gases at NTP. Source [16]

For a field of 30 kV/cm in the Thick-GEM hole region in Ar-CO₂ (70%-30%) mixture, Figure 4.17 gives us a gain of around 200 (but only if the foil was 1 cm thick). But assuming the Townsend coefficient varies linearly for different thicknesses, we expect a gain of the order of 10. Although the value might be approximate for that field, we can always vary the supplied voltage by around 1-2 kV/cm to achieve a similar value.

Thus, we predict a maximum of about 2200 primary electrons generated from one X-Ray, i.e., in one pulse. This corresponds to 0.3 fC of charge reaching the readout strips (~6250 electrons correspond to 1 fC), or 0.3 mV output from the preamplifier.

4.11.1 Simulation of Expected Gain

The results obtained using Figure 4.17 are for Argon-CO₂ (70%-30%) and (90%-10%) mixtures, whereas we have (70%-30%) and (80%-20%) mixtures available. To calculate the expected gain for an (80%-20%) mixture, and in a way, cross-check the theoretical calculations done, we performed simulations to calculate the expected gain for three different fields on Garfield++ using the nearly exact Boundary Element Method (neBEM) [17].

Garfield++ is a C++-based toolkit for the detailed simulation of particle detectors that use a gas mixture or a semiconductor material as the detector volume. Garfield++ needs electric field information (the electric field information can be imported to Garfield++ using Elmer [18], COMSOL [19], the neBEM package, etc.), transport properties of electrons in gas mixtures (calculated using Magboltz [20]), and the ionizations produced by relativistic charged particles (can simulated using HEED [21], SRIM [22], etc.). Several other classes help with simulating the initialization of particle tracks, avalanche and drift of the produced primary and secondary particles, and signal calculation.

The neBEM solver uses closed-form expressions of the potential and the field obtained from the symbolic integration of Green's function of a uniform charge density distributed over a triangular or rectangular boundary element. neBEM first breaks up the system of interest into right triangles and rectangles (they are referred to as primitives), and then the contribution from a primitive (assuming charge is uniformly distributed) is calculated using closed-form expressions (analytical solutions) of the potential and the field obtained from the symbolic integration of the Green's function.

For the detector setup we have used, a unit cell was made, and an image of the same is shown in Figure 4.18.

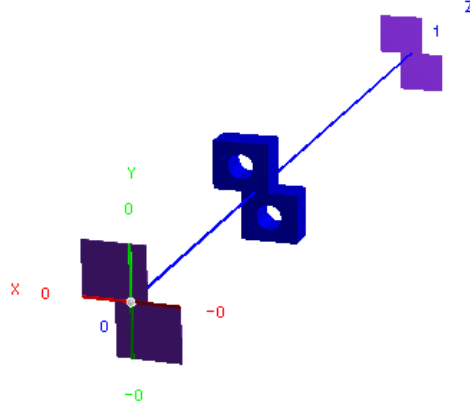


Figure 4.18: An image of the unit cell of the Thick-GEM setup.

The voltage biases supplied are shown in Table 4.3.

Entity	Voltage applied
Drift electrode	-2500 V
GEM top layer	-1500 V
GEM bottom layer	-500 V
Anode	0 V

Table 4.3: Voltages applied to the electrodes.

The corresponding plots of equi-potential lines are shown in Figures 4.19a and 4.19b.

The equi-potential lines appear to be distorted with something definitely going wrong. A report of this issue was sent to the authors of Garfield++ and neBEM. The setup currently in use has a Thick-GEM foil of pitch $450 \mu\text{m}$, and neBEM has only a limited number of solid structures for which electric fields can be calculated. The closest unit cell to that of the required detector with which we can obtain the expected plot of equi-potential lines can be done with a pitch value of $600 \mu\text{m}$ ⁶. An image of the unit cell of this setup is shown in Figure 4.20a and the plot of equi-potential lines that was obtained is as seen in Figure 4.20b. This unit cell is a solid cuboid with a lesser number of edges as compared to the

⁶we also need to note that since we will simulate gain, the new configuration is acceptable as the gain does not vary with pitch [23].

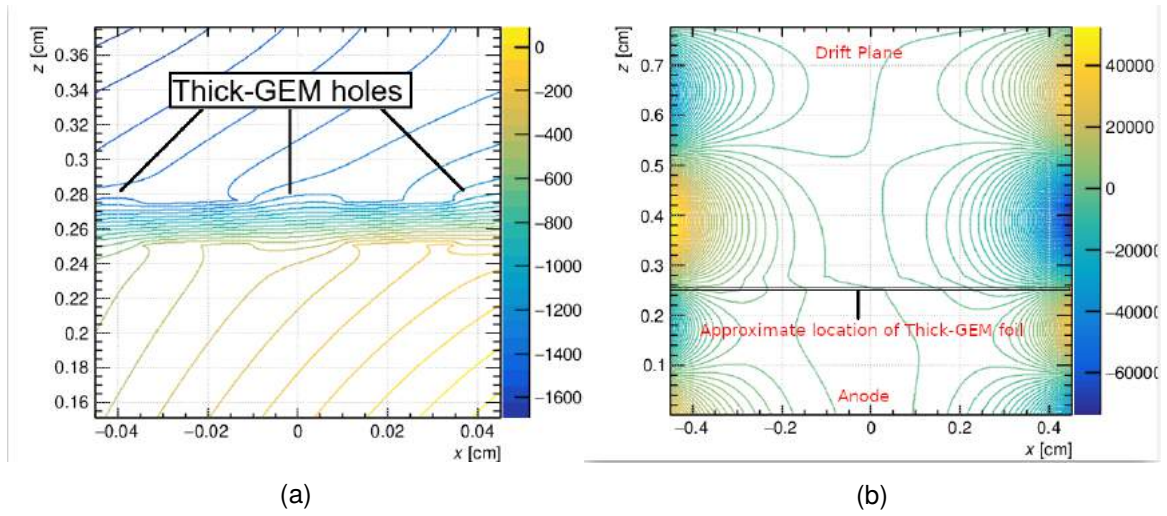


Figure 4.19: A plot of equi-potential lines (a) across the Thick-GEM foil (across three holes) and (b) across the full detector. The legend on the right for both images are potential values (in V). This was for 20 copies of the unit cell along X and Y directions each.

former unit cell and can be one of the possible reasons as to why this unit cell works and not the previous one.

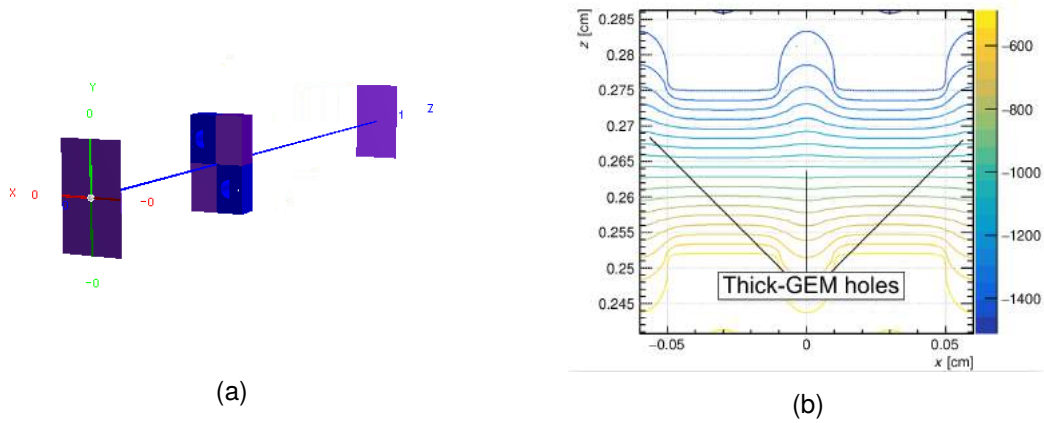


Figure 4.20: (a) An image of the unit cell of the Thick-GEM setup with a new pitch. (b) A plot of equi-potential lines across the Thick-GEM foil (across three holes). The legend on the right for both images are potential values (in V). This was for 20 copies of the unit cell along X and Y directions each.

We then simulated the gain for 1000 events where one event corresponds to an electron left in the drift region (0.25 cm above the Thick-GEM foil). This was done for 2 kV/cm

in the drift and induction region, and three different fields across the Thick-GEM foil (25 kV/cm, 30 kV/cm, and 35 kV/cm). The results thus obtained are shown in Table 4.4.

E_{hole} (kV/cm)	Gain
25	2.3
30	6.7
35	21

Table 4.4: The results of the simulated gain values for different electric fields in the Thick-GEM hole region (E_{hole}).

We see that the expected gain at 30 kV/cm match that of the prediction made in the previous section and that as we increase the field across the Thick-GEM holes, the gain increases. But we have a limit on the fields we can produce, as the capacitors in the low pass filters have an upper limit on the operating voltage. As will be explained in Section 4.13, this issue was resolved later. Overall, we expect the gain to increase as we increase the electric field in the Thick-GEM hole region.

Another interesting observation that was made through simulations is that we saw a drop in the field uniformity across these holes as one increases the voltage across the Thick-GEM foil. Figure 4.21a shows a contour plot of the electric field across the XY plane in the center of the Thick-GEM foil. We then plotted the electric field values across a line in the center of the hole parallel to the X-axis (See red line in Figure 4.21a). This was done for different field values across the Thick-GEM foil, and a plot of the same is shown in Figure 4.21b. We see that at higher fields, there is a dip in the field at the center of the hole, which means that increasing voltage bias across the Thick-GEM foil also involves a loss in the electric field uniformity in the holes.

Apart from field uniformity, we also studied the collection and extraction efficiency as a function of different electric fields in the drift and hole regions. The electric field in the drift, hole and induction regions are denoted as E_{drift} , E_{hole} , and E_{ind} , respectively. If the number of electrons generated in the drift volume and have reached the Thick-GEM hole is denoted as N_{hole} and the number of electrons generated in the drift volume is denoted as N_{drift} , then the collection efficiency is defined as:

$$\text{CE} = \frac{N_{\text{hole}}}{N_{\text{drift}}} \quad (4.1)$$

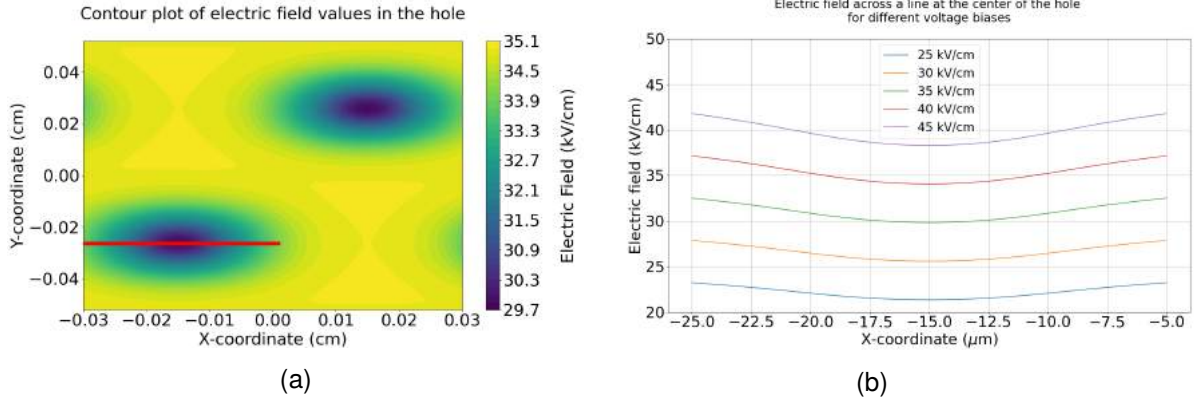


Figure 4.21: (a) Contour plot of the electric field across the XY-plane in the center of the Thick-GEM foil (35 kV/cm). (b) Electric field values across a line in the center of the hole parallel to the X-axis.

We require this value to be high as this ensures that all the electrons created in the drift volume are collected and sent drifting through the hole.

Apart from a high collection efficiency, we also need Extraction Efficiency (EE) to be high, where EE is defined as:

$$EE = \frac{N_{\text{hole}}}{N_{\text{ind}}} \quad (4.2)$$

where N_{ind} is the number of electrons generated in the hole region and have reached the induction region.

CE and EE get us to the effective gain of the detector (G_{eff}), which is defined as:

$$G_{\text{eff}} = G \times CE \times EE \times N_{\text{primary}} \quad (4.3)$$

where G is the ideal gain of the detector and N_{primary} is the number of primary electrons generated in the detector volume. Maximizing CE gets us to a low EE (and thus low G_{eff}), and maximizing EE gets us to a low CE (and thus low G_{eff}). We thus need to operate the detector where the product of CE and EE is maximum.

The obtained simulation results of the variation of CE and EE with $E_{\text{drift}}/E_{\text{hole}}$ were plotted and the same is shown in Figure 4.22.

Using the above results from simulations, we operated the detector at voltages that we expect to give the best gains, and we did not observe a signal. The expected amplitude of the signal we expect from the preamplifier is of the order of 1 mV, whereas we are currently getting a noise of about ~200 mV (See Figure 4.24), which is too high for the signal we are

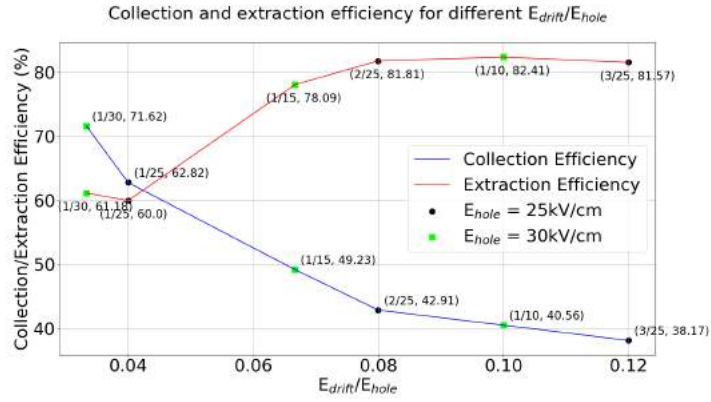


Figure 4.22: A plot of collection and extraction efficiency for different E_{drift}/E_{hole} values. This simulation was done for two different E_{hole} values (25 and 30 kV/cm) and three different E_{drift} values (1, 2, and 3 kV/cm). The coordinates in the plots adjacent to the points correspond to $(E_{drift}/E_{hole}, CE \text{ or } EE)$.

expecting, thus establishing a severe need to find ways to reduce noise or increase the gain of the detector.

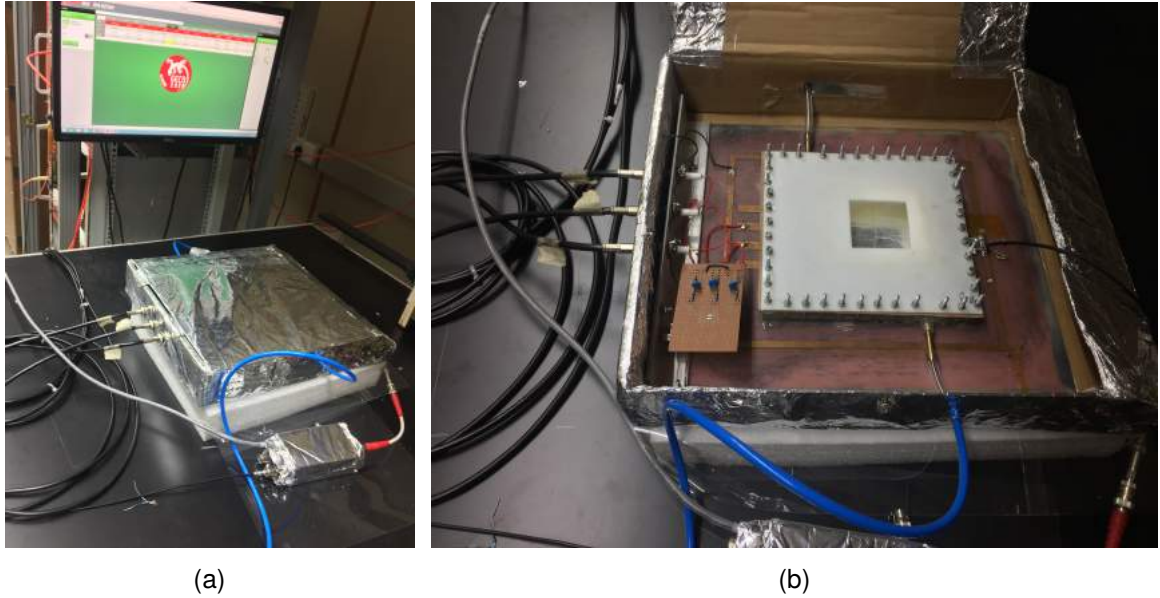


Figure 4.23: (a) An image of the detector inside the Faraday's cage. (b) A view of the detector inside the Faraday's cage.

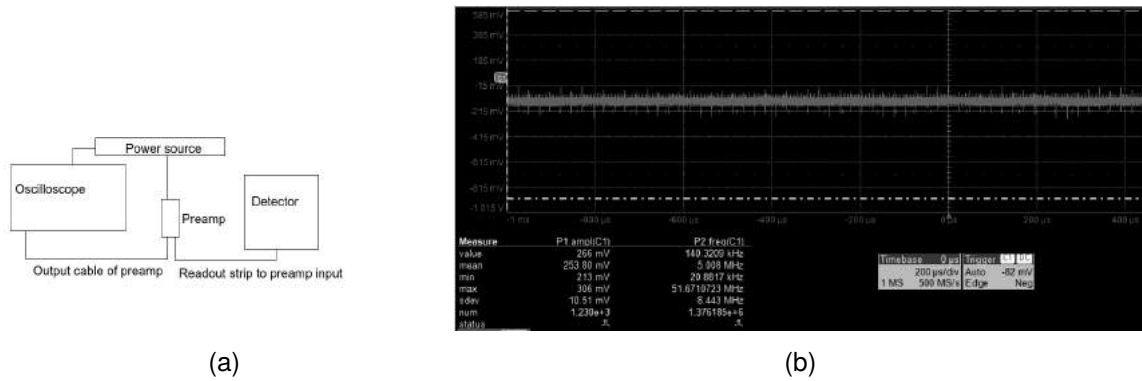


Figure 4.24: (a) The schematic circuit diagram to measure noise from the preamplifier connected to readout strips of the detector and (b) the corresponding output of the preamplifier.

4.12 Noise Reduction

After performing simulations and a simple theoretical calculation, we found that the expected signal amplitude is much lower than compared to the noises we are observing. One way to improve the signal/noise ratio is by decreasing noise.

An outer rectangular copper strip can be seen Figure 4.5. This connection was made to provide points for ground connections. All grounds were made common using this strip, including the HV supply ground and the connection from the readout strip. But with a signal containing charges of the order of fCs, a disturbance in the ground⁷ can affect the signal and induce noise. For this reason, we need to build a separate ground point using a large metal plate or a very long and thick wire bundle so that it can act as a secondary ground, and given that we know there would not be disturbances from other appliances in the building, this would serve as a stable ground for us. There was access to a chemical ground that was utilized for grounding the detectors.

The following steps were implemented, which had an effect on reducing the noise:

1. To reduce the effect of stray electromagnetic radiations on the detector output, a Faraday cage was built inside which the detector was placed. See Figures 4.23a and 4.23b.
2. We started grounding components to a chemical ground using thick Aluminum braids.

⁷This ground is the same one used for all ground connections in the building. Thus other appliances connected to this ground can alter the ground levels.

We grounded the preamplifier connections, high-voltage connections, and the ground of the detector to the chemical ground. This brought down the noise from 200 mV to about 15 mV (See Figure 4.26a).

3. Then, some minor tweaks were done to help with noise reduction. The gas nozzles and the screws used to make the gas-tight detector were seen to act as antennas, so they were grounded. Additionally, grounding the preamplifier body and the Faraday cage helped in reducing the noise from 15 mV to around 6 mV (See Figure 4.26b).

An image of the setup after all the steps was implemented is shown in Figure 4.25.

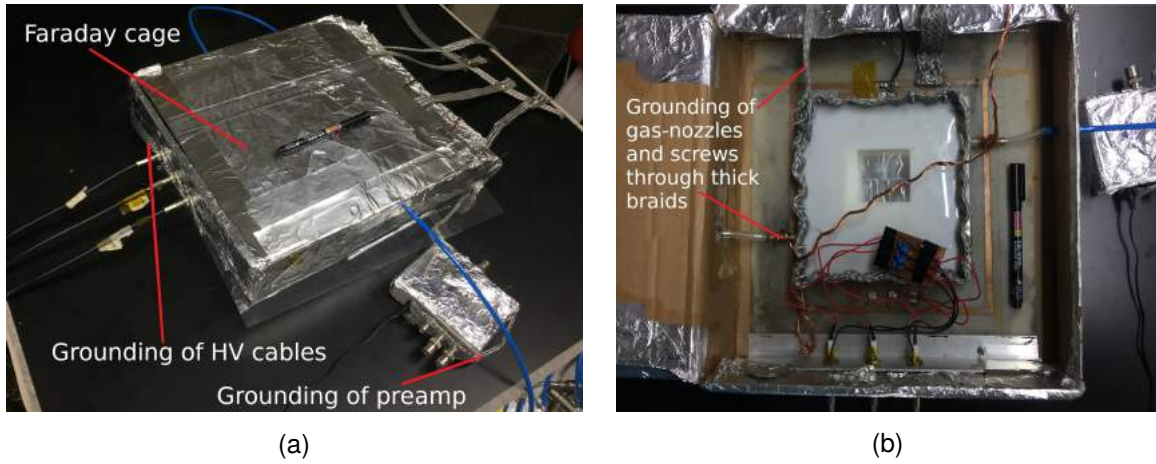


Figure 4.25: Images of the detector setup after steps were taken to reduce noise.

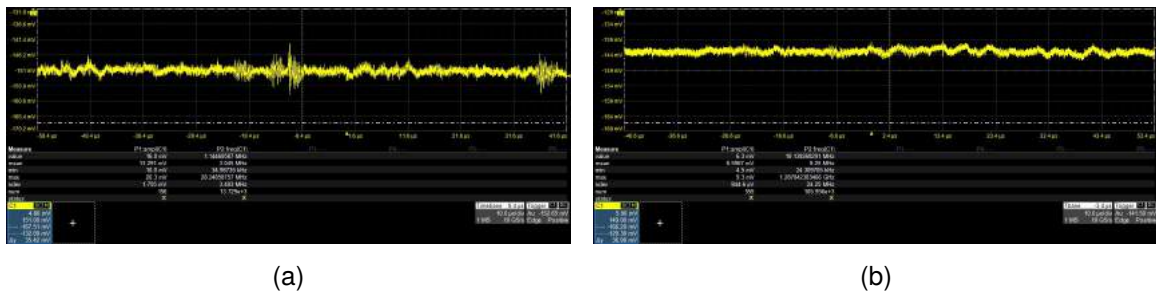


Figure 4.26: Noise observed from the preamplifier at different stages of attempts to reduce the noise. A noise of about 15 mV is seen in (a) and about 6 mV in (b).

Finally, we also noted that the noise from the detector was of the order of 2 mV after all the steps were taken to reduce the noise, which means a good amount of noise is also being picked up by the preamplifier. An image showing the same is shown in Figure 4.27.

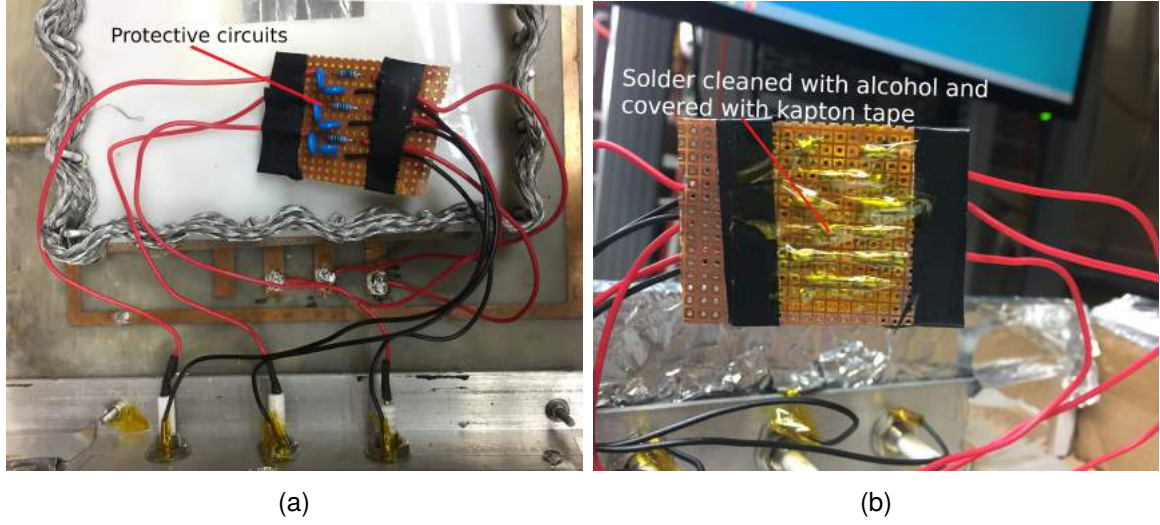


Figure 4.28: Images of (a) front side and (b) backside of the well-soldered and cleaned protective circuit made in a way to have minimum leakage in current.

V	I_{bottom} (nA)	I_{top} (nA)	I_{drift} (nA)
-500	33.8	19.6	65.5
-750	63.2	34.8	113.2
-1000	94	54.5	172.4
-1250	125.2	90.8	231.3
-1500	165.3	121.1	318.2
-1750	207.7	156.7	404
-2000	261	203	506.6
-2250	—	Sparking	—

Table 4.5: The leak current in the circuits for the three terminals for the corresponding voltage applied. I_{bottom} , I_{top} , and I_{drift} correspond to the current in the lower Thick-GEM, upper Thick-GEM, and drift electrode circuits, respectively.

V	I_{bottom} (nA)	I_{top} (nA)	I_{drift} (nA)
-500	3.4	2.1	14.9
-750	6.5	2.9	22.8
-1000	9.9	5.5	37.1
-1250	13.8	6.8	48.1
-1500	18	10	65.7

Table 4.6: The leak current in the circuits after careful construction and precautions. An image of the corresponding circuit is as seen in 4.28. The values marked in red are above the accepted limit.

V	I_{bottom} (nA)	I_{top} (nA)	I_{drift} (nA)
-500	1.1	0.0	0.4
-750	0.7	0.2	0.5
-1000	0.2	0.2	1.1
-1250	0.5	0.2	1.2
-1500	0.3	0.3	1.8

Table 4.7: The leak current in the circuits after the removal of the low pass filter.

4.14 Increasing Signal Amplitude

Apart from decreasing noise, the other way to improve the signal/noise ratio is by increasing the signal amplitude (by increasing the effective gain of the detector). We had procured three Thick-GEMs from Micropack Pvt. Ltd. and all of them are of the same configuration (different specifications give different gains). Thus we are left with three other ways to increase the gain of the detector:

1. By changing the gas mixtures: Lesser amounts of quenching gas would mean greater amplification. Until now, we have tried two different gas mixtures: Ar-CO₂ (70%-30%) and Ar-CO₂ (80%-20%), both giving no observable signal for the ⁵⁵Fe source.
2. Using multiple Thick-GEM foils to increase the gain of the detector: This is done by stacking multiple foils, one above the other, with the readout and drift electrode at the bottom and top, respectively, as usual. But the etching process we did had four electrodes included that can be used to provide a bias to the electrodes inside the gas-tight setup. For housing multiple Thick-GEM foils, we would need to etch a new PCB board as the current board was not designed to be capable to house multiple Thick-GEM foils (To house multiple foils, one needs multiple strips to supply the voltages to the electrodes). Thus, a restart of the entire detector fabrication process is something that is not possible in the given time frame.
3. Increasing the electric field.

For the Ar-CO₂ (80%-20%) gas mixture, and after imposing the changes to minimize noise and leak currents, we were able to observe a signal at high electric fields. For voltages, -500 V, -1640 V, and -2140 V supplied to the bottom Thick-GEM layer, top Thick-GEM

layer, and drift electrode respectively, the preamplifier, amplifier, and MCA output are shown in Figures 4.29a, 4.29b, and 4.30.



Figure 4.29: For an ^{55}Fe source, the output from the (a) preamplifier and (b) amplifier that was observed with an oscilloscope. Here the X-Axis is the time, and the Y-Axis is the voltage.

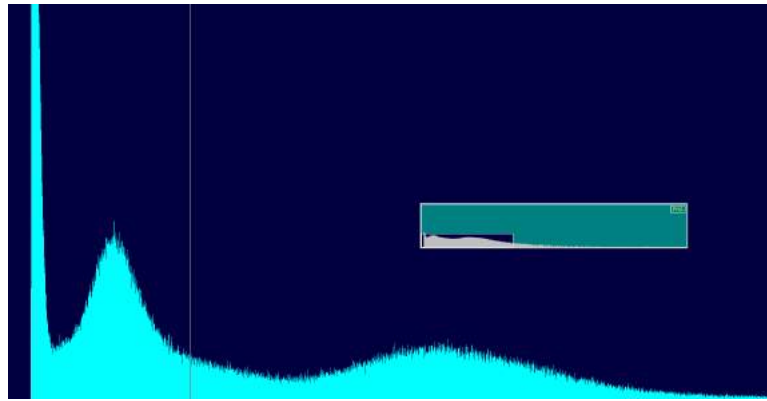


Figure 4.30: The MCA output for an ^{55}Fe source placed in front of the Thick-GEM detector. Here the X-Axis is the channel number, and the Y-Axis is the counts.

The spectrum to the left-most region of the spectrum is noise. An interesting observation is that the main emission line for the ^{55}Fe source is at 5.9 keV and thus the spectrum should have one main peak, but we see two peaks in Figure 4.30. If there is a good resolution, one can see a second peak to the left of the main peak, called the Argon escape peak, which originates when the 5.9 keV X-Ray extracts an electron from the inner K-shell of the Argon atom and the vacancy is filled by an outer electron, with the emission of another X-Ray of energy 2.9 keV. The two peaks we are seeing in Figure 4.30 do not correspond to the main emission line and Argon escape peak as the escape peak will have lesser counts than the peak corresponding to the 5.9 keV X-Ray. Reasons for observing two peaks are still under investigation. We believe that this could be because of a bend in the Thick-GEM foil due to

the misalignment of the holes that hold the foil in the detector volume. As a double-check, we also placed a Strontium (^{90}Sr) source and observed a spectrum characteristic to that of a beta source - a continuous energy spectrum.

4.15 Characterization of the Thick-GEM Detector

Considering the left peak as our main peak, we characterized our detector. We first plotted the variation of the effective gain with the voltage bias applied across the Thick-GEM foil. The same has been shown in Figure 4.31. The gain is defined as:

$$\text{Gain} = \frac{\text{Total Pulse Amplitude}}{\text{Number of Primary Electrons (= 0.033 fC)}} \quad (4.4)$$

where the number of primary electrons is calculated theoretically (we calculate the total number of electrons the 5.9 keV X-Ray from the ^{55}Fe source can generate, using the ionization values of Argon and CO_2 and their amount in the gas volume). The MCA output was calibrated using a test pulse generator which helps us obtain the pulse amplitude using the channel number. We found that for the setup we used, charge generated = $0.022 \times \text{Channel No.} = 3.513 \text{ fC}$.

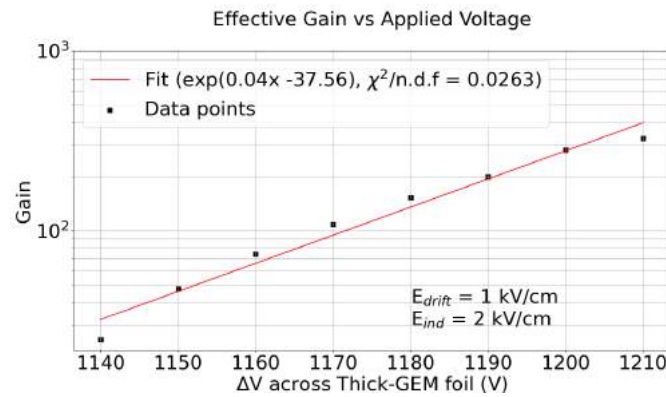


Figure 4.31: A plot of the effective gain vs. voltage bias across the Thick-GEM foil.

For voltage biases below 1140 V, the spectrum was hidden under the noise, and for voltage biases above 1210 V, the detector started sparking, hence gains in these voltage biases were not calculated.

For the main peak in the spectrum, the Full-Width at Half Maximum (FWHM) is given by:

$$\text{FWHM} = 2 \times \sqrt{2 \times \ln(2)} \times \sigma \quad (4.5)$$

where σ is the standard deviation of the Gaussian.

Using FWHM, one defines resolution as:

$$\text{Resolution (\%)} = \frac{\text{FWHM}}{E} \quad (4.6)$$

where E is the related energy of the peak and corresponds to the peak centroid in the MCA output. A plot of resolution vs. the voltage bias applied across the Thick-GEM foil is shown in Figure 4.32.

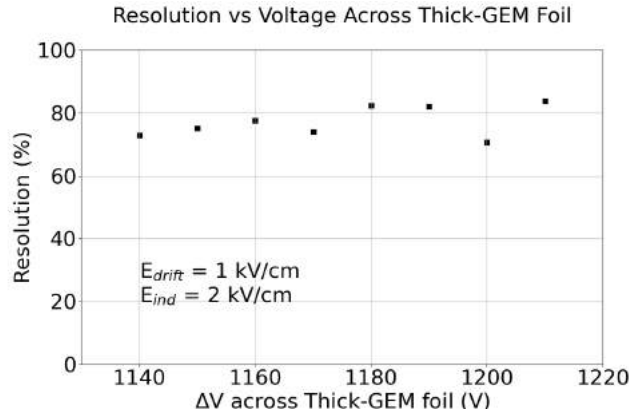


Figure 4.32: A plot of resolution vs. voltage bias across the Thick-GEM foil.

We then looked at how the total count rate varies with the drift and induction fields, and plots of the same are shown in Figures 4.33a and 4.33b.

In Figure 4.33a, there are three different regions that can be observed. The low rate at low drift fields is because the electrons generated in the drift region do not reach the holes. The plateau in the moderate drift fields is where this detector needs to be operated. Finally, the drop in count rate after a certain value of the drift field is because the electrons generated in the drift region achieve enough velocities to hit the top electrode of the Thick-GEM foil, instead of drifting into the holes.

In Figure 4.33b, the count rate at low induction fields is because the electrons coming out of the holes do not reach the readout strips, instead, they drift towards the bottom layer

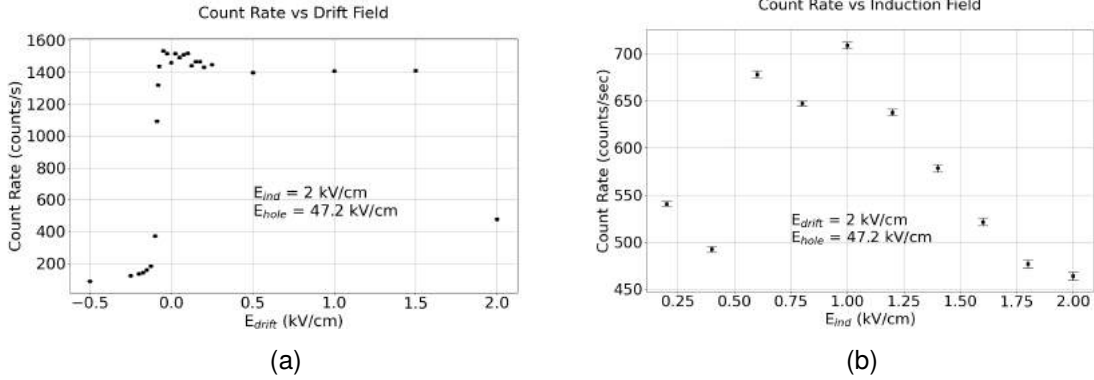


Figure 4.33: Plots of the variation of count rate with the (a) drift and (b) induction fields.

of the Thick-GEM foil. The optimum induction field value to operate the detector is around 1 keV as it corresponds to the highest count rate. We also see that as we increase the induction field beyond this point, the count rate drops as for these field values, there is a distortion in the electric field lines in the hole and induction region.

4.16 Gain Evolution in the Thick-GEM Detector

Another interesting study that was done with the Thick-GEM detector was to see the effect of sustained exposure to the ^{55}Fe source on the detector gain. A stable gain is desired while performing experiments with the detector, and a study on how the gain evolves over time would give us information about when the detector will reach stable gain values. We left the detector running for 7 hours, with the MCA running on a macro file. Signs of the dropping gain can also be observed with the MCA output (See Figure 4.34). The final output of the variation of gain with time is shown in Figure 4.35.

We observe that over time, there is a drop in the gain values, and the reasons for this are due to charging up, and temperature and pressure changes in the environment. We were not able to perform a study for a longer duration as we were concerned with the room temperature rising, which could damage equipment if left unsupervised during the night.

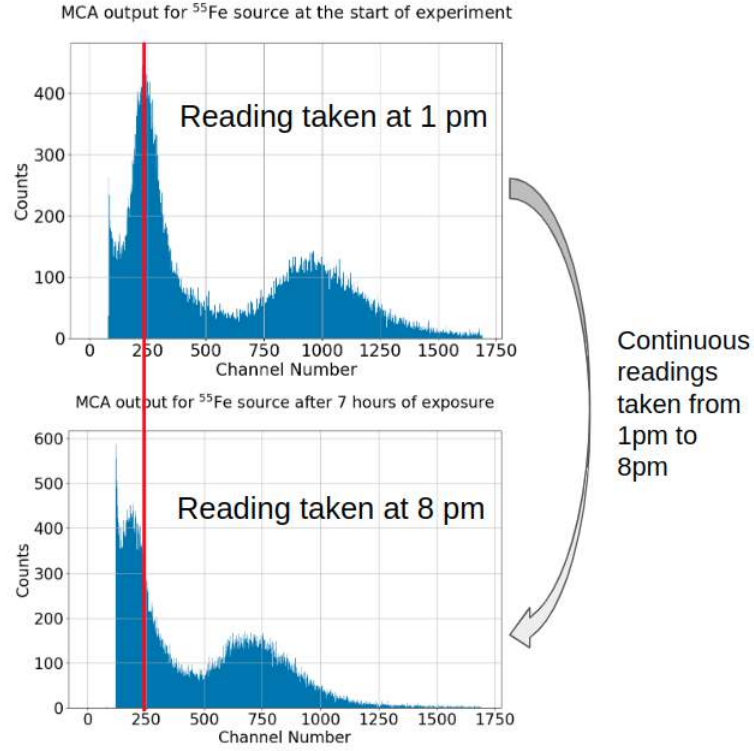


Figure 4.34: The shift in the peak of the MCA spectrums obtained at two different times during the continuous exposure to radiation. The shift in centroid shows the drop in the detector gain over time.

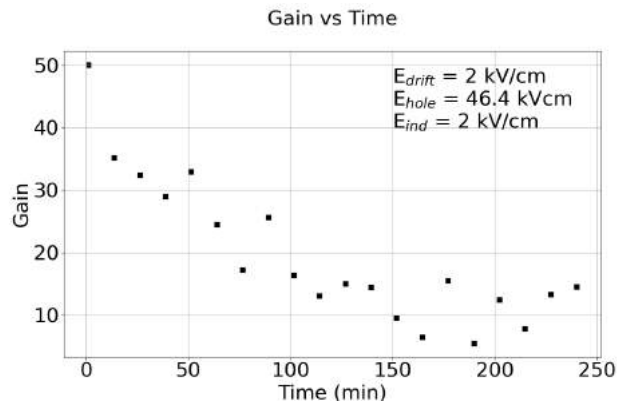


Figure 4.35: The evolution of gain over time for the Thick-GEM detector.

Chapter 5

Development of the Proportional Counter

5.1 Overview

This Chapter will deal with the details of the work done to fabricate and characterize a proportional counter and discuss the results obtained from a few simulations performed using Garfield++. The testing process of the Thick-GEM, as we saw in Chapter 4 requires effectively extracting pulses of charges of low magnitude and, at the same time, minimizing noise to the Femto-coulomb or sub-Femto-coulomb range. The motive to make and test a detector like a proportional counter is to introduce the importance of gain and noise reduction. The Thick-GEM detector is susceptible to noise and the charge of noise pulses is in the Femto coulomb range. In contrast, the proportional counter can achieve high gains with similar voltage biases applied. Making the proportional counter work also gave us another handle to test the electronic chain.

The proportional counter comprises a thin anode wire, a grounded cylinder circumscribing this wire, and a window transparent to incoming particles. There is a gas mixture flowing inside the detector volume. P-10 gas ($\text{Ar}+\text{CH}_4$ (90%+10%)) was the gas that was used. The electric field inside the proportional counter is as given in Equation 3.5. As one gets closer to the anode wire, the electric field magnitude increases, and the avalanches occur around the wire. The following components are needed to construct the detector fully:

- Outer Cylinder
- Thin anode wire
- End caps for gas-tight connection
- Electronics

5.2 Design and Fabrication

The proportional counter is a simple detector to fabricate. The only challenge is to have a tight wire inside the cylinder while maintaining a gas-tight setup with the end caps. We cut an Aluminum tube to make the outer cylinder, a copper strand that can be found in regular wires as the anode wire, and a 3D printed component as the end caps.

The outer cylinder was from an Aluminum tube of diameter 1.9 cm, and the length of the cut tube was 15 cm. A small rectangular window was cut using a drill with a cutting disk in this outer cylinder. To make the cylinder gas-tight, we used Kapton tape to cover this window, through which the incident radiation enters.

The end caps were designed on AutoCAD and printed using the 3D printer available in the Robotics Laboratory at NISER. These caps also had two tubes protruding to serve as the inlet and outlet pipes for the gas to flow through. Images of the same are shown in Figures 5.1a and 5.1b.

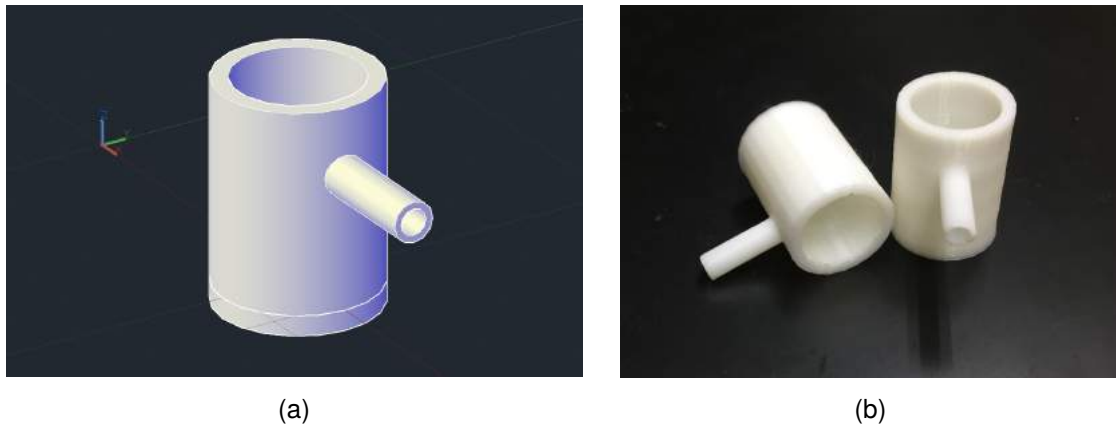


Figure 5.1: Image of (a) the end cap designed on AutoCAD and (b) the 3D printed end caps.

The anode wire taken from the copper strands present in regular wires was of thickness 0.027 cm. There were no holes made in the end caps so that the wire could go through as the printer does not have the capabilities of printing objects of dimensions of 0.05 mm order. But one important process for a 3D printer to work is that the resin is melted and molded into shapes, which is what makes the printer create objects of the desired designs and shapes. This meant that we could heat the wire and make it pass through the end caps through a hole of the size of its diameter. We applied glue on the outside to ensure there

was no leak. The wire coming out was then connected to the preamplifier (through an SHV connector) and further electronics. An image of the detector at this stage is shown in Figure 5.2a.

The electronics chain is exactly the same as that of the Thick-GEM, i.e., we have used a 142IH Ortec preamplifier, a CAEN N968 Spectroscopy Amplifier, and an Ortec 927 ASPEC MCA.

Although the proportional counter has a high gain, the noises we were initially observing were very high and were a 50 Hz noise from some electrical component in the building. To reduce the same, we grounded the outer body of the preamplifier and made a Faraday cage that housed the detector. An image of the same is shown in Figure 5.2b. This was sufficient to bring down the noises to a level where we could observe the signal. This shows how careful one needs to be while operating a Thick-GEM detector compared to the proportional counter.

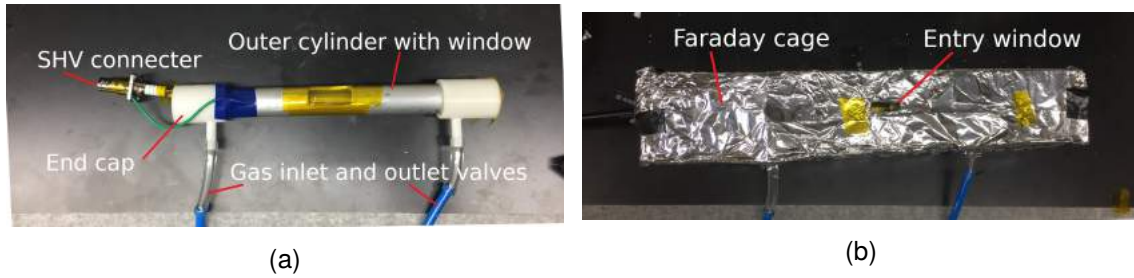


Figure 5.2: An image of (a) the proportional counter built and (b) the detector placed in a Faraday cage.

5.3 Initial Checks

For a voltage of 2800 V supplied to the anode wire, and after placing an ^{55}Fe source, we observed the outputs of the preamplifier, the amplifier, and the MCA output. The same has been shown in Figures 5.3a, 5.3a and 5.4.

We observe that we have obtained the desired characteristic 5.9 keV peak of the Iron source and the Argon escape peak to the left. We now will move forward to performing a characterization of the proportional counter.

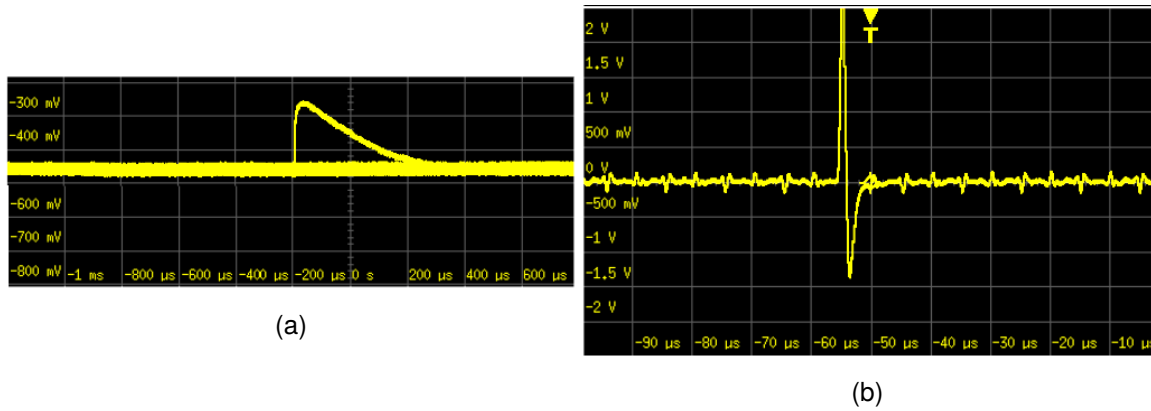


Figure 5.3: For an ^{55}Fe source, the output from the (a) preamplifier and (b) amplifier that was observed with an oscilloscope. Here the X-Axis is the time, and the Y-Axis is the voltage.

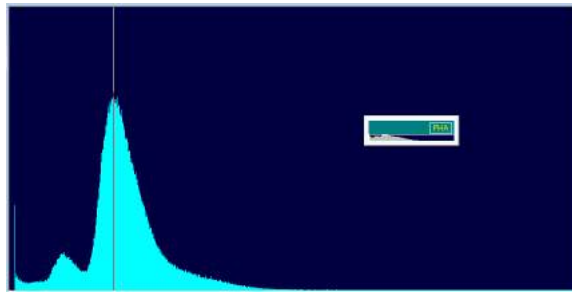


Figure 5.4: The MCA output for an ^{55}Fe source placed in front of the proportional counter. Here the X-Axis is the channel number, and the Y-Axis is the counts.

5.4 Characterization of the Proportional Counter

It is desirable that a detector is operating in a configuration with the least resolution. The resolution varies with the voltage supplied to the anode wire for proportional counters. After placing the source, we obtained the spectra for a specific voltage and subtracted them from the spectra obtained without the source (background). This was done for different voltages, thus giving us a plot of resolution vs. voltage supplied to the anode wire. The plot of the same is shown in Figure 5.5.

The region to the left of 2610 V is where the signal is hidden under the noise, and the region above 2850 V is where the voltage supplied is too high, leading to sparking. We see that the proportional counter we built performs best when a voltage of 2670V is given to the anode wire. For voltages beyond 2850V, we observed sparks in the proportional counter,

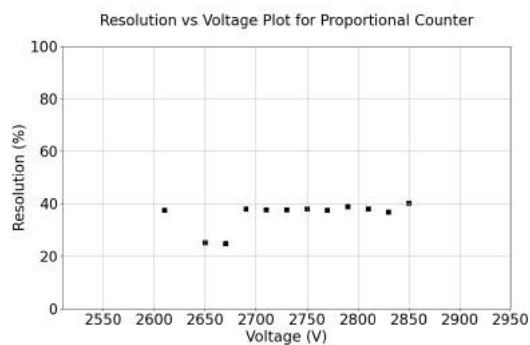


Figure 5.5: The plot of resolution vs. voltage applied to the anode wire.

and an image of the same is shown in Figure 5.6.

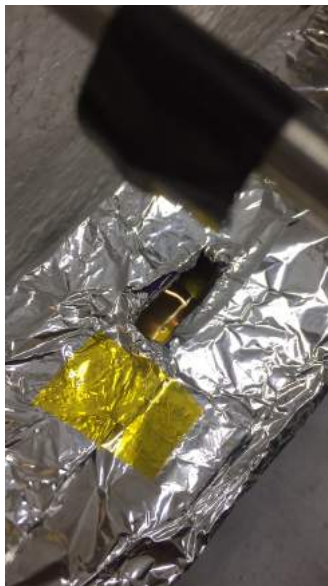


Figure 5.6: An image captured when the proportional counter was sparking.

5.5 Operating at Negative Voltage

Proportional counters always have a positive voltage to the anode wire and grounded outer cylinder. Let us refer to this configuration as the positive-voltage configuration. One question to ask is why is it always in this configuration (a positive voltage to the anode and grounding of the cylinder)?

Suppose one grounds the anode wire and a positive voltage to the cylinder. In that case, the electric field inside will not reach the required levels to produce sufficient multiplication for a readable output. This can be done through a simple calculation similar to what was done to derive Equation 3.5.

Let us refer to the setup wherein the anode wire is given a negative voltage (and the cylinder grounded) as the negative-voltage configuration. The electric field magnitude would be the same but opposite in direction compared to that of the positive-voltage configuration. When an ionizing radiation enters the detector volume in the positive-voltage configuration, electrons drift towards the anode, and as they get closer, the field increases. The majority of the ions are formed near the wire, and they drift towards the cylinder walls; given the slow speed of the ions and having to traverse a long distance, the pulse has a long tail. Appendix A.3 goes into the equations involved in the charge pulse output. It is desirable to have a short tail. Thus the advantage of operating the proportional counter in the negative-voltage configuration is that we predict a shortening of the pulse's tail as the ions will have to drift much smaller distances.

Upon testing the same, we got no signal, as seen in Figure 5.7. The gain in this mode of operation is expected to be low and hence does not produce a large signal compared to what was produced in the positive-voltage configuration. This is because in the positive-voltage configuration, as the primary electrons drift towards the wire and hence higher fields, they ionize further atoms, electrons from which ionize further atoms, and so on. In the negative-voltage configuration, the electrons drift towards the cylinder and towards regions where the field is lower, thus not giving rise to a big enough avalanche effect to produce a readable signal.

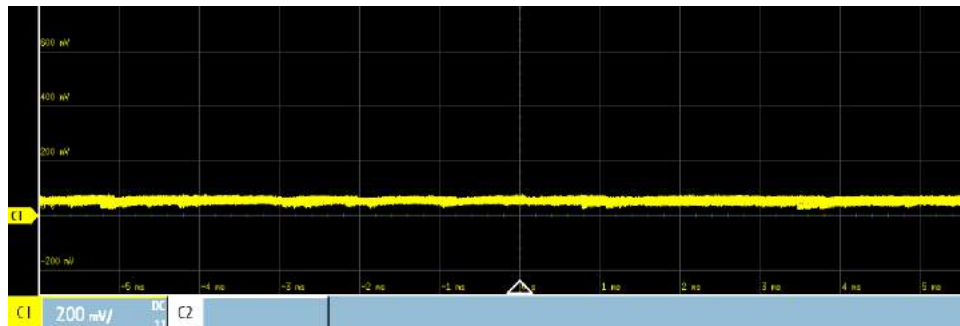


Figure 5.7: For an ^{55}Fe source, the preamplifier output of the proportional counter in the negative-voltage configuration. Here the X-Axis is the time, and the Y-Axis is the voltage.

To confirm the statement made in the previous paragraph, we simulated a proportional counter similar to what was used in the experiment using Garfield++ and the neBEM package. There is no tube-like structure in the geometries that neBEM can discretize, instead, we made a cuboid structure instead of the outer cylinder. neBEM does have a pre-defined wire geometry and we used one that is exactly similar to that of the one used in the experiment. We simulated the gain for both the negative and positive-voltage configuration for 1000 events. Here one event corresponds to an electron left in the cylindrical volume. The positive-voltage and negative-voltage configurations were found to have a gain of 4205 and 1.39 respectively. The gain for the positive-voltage configuration is three orders higher than that of the negative-voltage configuration, which confirms the statement made in the previous paragraph.

As seen through simulations and experiments, the gain of the proportional counter is typically of the order of 10^3 and that of Thick-GEMs is around 10^2 , which means that one has to look at noise more carefully in a Thick-GEM compared to the proportional counter. The electric field in the holes of the Thick-GEM is governed by the foil thickness and the voltage bias applied, whereas the electric field near the wire in a proportional counter can reach very high values. Another advantage of the proportional counter is that it has a reduced ion-backflow and there is almost no trapping of ions that can distort the electric field, as it occurs in Thick-GEMs. But the proportional counter is a detector that can easily shift to working in the GM region, depending on the voltage bias applied, whereas this is not the case in Thick-GEMs.

5.6 Gain Evolution in the Proportional Counter

A study of the effect of continuous exposure to the ^{55}Fe source on the detector gain, was performed. We left the detector running for 16 hours, with the MCA running on a macro. The macro code commanded the MCA to take the spectrum data for 59 seconds and save the spectrum in a file. The data-taking process would again begin once the next minute begins. This was done for 999 minutes, amounting to about 16 hours' worth of data-taking. The MCA output was calibrated using a test pulse generator and given we approximately find the number of primary ionizations produced in the volume (similar to calculations done in Section 4.11), we can relate the channel number to the charge of the signal pulse. We

found that for the setup we used, the charge generated = $0.056 \times \text{Channel_No.} + 0.467$ (fC). By a simple calculation, we can calculate the expected number of primary electrons produced (~ 0.039 fC) for the gas mixture we are using, and we can thus obtain the gain of the detector for every minute of the data-taking process. Signs of the dropping gain can also be observed with the MCA output (See Figure 5.8). The final output of the variation of gain with time is shown in Figure 5.9.

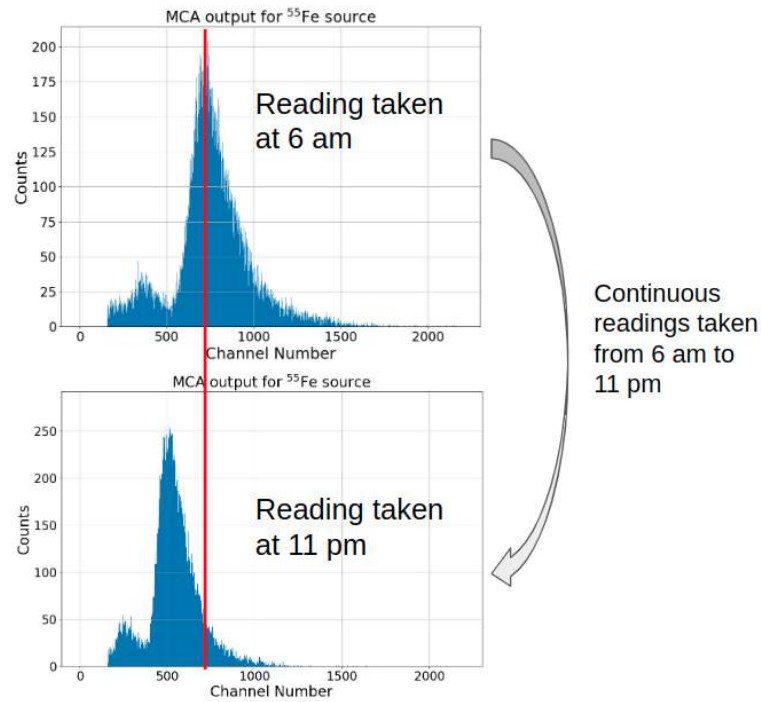


Figure 5.8: The shift in the peak of the MCA spectrums obtained at two different times during the continuous exposure to radiation. The shift in centroid shows the drop in the detector gain over time.

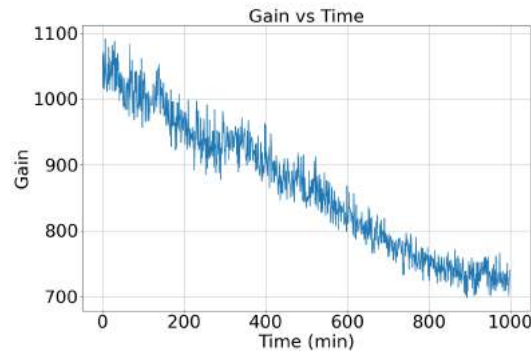


Figure 5.9: A plot of the variation of gain with time to demonstrate the drop in gain in the proportional counter upon continuous radiation exposure.

We see that the gain value drops over a period of 16 hours, and this drop can be due to space-charge effects and changes in temperature and pressure.

Chapter 6

Conclusion and Outlook

During the entirety of the academic year, the concepts of interaction of radiation and matter, and the working principles of gaseous radiation detectors were learned. The skills pertaining to designing and fabricating a Thick-GEM detector from scratch were learned. We successfully constructed and assembled the detector and performed some preliminary tests. The observations of the same have been described in Chapter 4. Garfield++ simulations were performed to study the gain, field uniformity, and collection and extraction efficiency, results of which were used to find an optimum configuration to operate the detector in. The noise levels were brought down from 200 mV to 6 mV, and the leak current was brought down to less than 20 nA for a supply of 500 V. After controlling the noise and the leak currents, we observed a signal upon placing an ^{55}Fe source. Further studies on the characterization and gain evolution were done for the Thick-GEM detector.

A proportional counter was built to validate the electronics chain and also show the ease in producing a signal with a detector capable of producing high gains, as compared to a sophisticated detector like the Thick-GEM. The detector was characterized and the working principle of the proportional counter was better learned through Garfield++ simulations and by operating the detector with a negative bias to the anode wire. Finally, a study on the evolution of gain of the detector over time upon continuous exposure to radiation was performed.

Bibliography

- [1] William R. Leo. *Techniques for Nuclear and Particle Physics Experiments: A How-to Approach*. 2nd. Springer, 1994. ISBN: 3540572805, 9783540572800.
- [2] S.S. Kapoor and V.S. Ramamurthy. *Nuclear Radiation Detectors*. New Age International Publishers, 1986. ISBN: 9780852264966. URL: <https://books.google.co.in/books?id=RX5Xdo030X0C>.
- [3] Theopisti Dafni. “A Search for Solar Axions with the MICROMEGAS Detector in CAST”. PhD thesis. Darmstadt, Tech. U., Oct. 2008.
- [4] M.A. Chefdeville. “Development of micromegas-like gaseous detectors using a pixel readout chip as collecting anode”. Undefined. PhD thesis. University of Amsterdam, Jan. 2009. ISBN: not assigned.
- [5] Fabio Sauli. *Gaseous Radiation Detectors: Fundamentals and Applications*. Cambridge Monographs on Particle Physics, Nuclear Physics and Cosmology. Cambridge University Press, 2014. DOI: 10.1017/CB09781107337701.
- [6] F. Sauli. “GEM: A new concept for electron amplification in gas detectors”. *Nuclear Instruments and Methods in Physics Research Section A: Accelerators, Spectrometers, Detectors and Associated Equipment* 386.2 (1997), pp. 531–534. ISSN: 0168-9002. DOI: [https://doi.org/10.1016/S0168-9002\(96\)01172-2](https://doi.org/10.1016/S0168-9002(96)01172-2). URL: <https://www.sciencedirect.com/science/article/pii/S0168900296011722>.
- [7] A. Breskin et al. “A concise review on THGEM detectors”. *Nuclear Instruments and Methods in Physics Research Section A: Accelerators, Spectrometers, Detectors and Associated Equipment* 598.1 (2009). Instrumentation for Colliding Beam Physics, pp. 107–111. ISSN: 0168-9002. DOI: <https://doi.org/10.1016/j.nima.2008.08.062>. URL: <https://www.sciencedirect.com/science/article/pii/S0168900208012047>.
- [8] Ibrahim Alsamak et al. *Garfield++*. URL: <https://garfieldpp.web.cern.ch/garfieldpp/>.

- [9] AN Zheng-Hua et al. *Experimental study on the performance of a single-THGEM gas detector*. 2010. DOI: 10.1088/1674-1137/34/1/015. URL: <http://hepnp.ihep.ac.cn/article/id/b539b7ac-61f5-4e38-9627-6ed91572ee8f>.
- [10] S Bressler et al. "Recent advances with THGEM detectors". *Journal of Instrumentation* 8.12 (2013), C12012–C12012. ISSN: 1748-0221. DOI: 10.1088/1748-0221/8/12/c12012. URL: <http://dx.doi.org/10.1088/1748-0221/8/12/C12012>.
- [11] John H. Moore et al. *Building Scientific Apparatus*. 4th ed. Cambridge University Press, 2009. ISBN: 0521878586,9780521878586.
- [12] *Preamplifier Introduction*. URL: <https://www.ortec-online.com/-/media/ametektortec/other/preamplifier-introduction.pdf>.
- [13] *Technical Information Manual MOD. N968 Spectroscopy Amplifier*. URL: <https://www.caen.it/products/n968/>.
- [14] Andrew Boston. *Pulse Processing: Pulse Shaping*. URL: https://ns.ph.liv.ac.uk/~ajb/ukgs_nis/pre-course-material/lec2-03.pdf.
- [15] Tutor L. Benussi. *GEM detector construction and characterization*. INFN, Frascati, Italy, Oct. 2015. URL: <https://agenda.infn.it/event/9123/contributions/77376/attachments/56136/66279/EDIT2015Benussi.pdf>.
- [16] P. A. Zyla et al. "Review of Particle Physics". *PTEP* 2020.8 (2020), p. 083C01. DOI: 10.1093/ptep/ptaa104.
- [17] Supratik Mukhopadhyay and Nayana Majumdar. *A nearly exact Boundary Element Method*. URL: <http://nebem.web.cern.ch/nebem/>.
- [18] *Elmer FEM, open source multiphysical simulation software*. URL: <http://www.elmerfem.org/blog/>.
- [19] *COMSOL Multiphysics Simulation Software*. URL: <https://www.comsol.com/comsol-multiphysics>.
- [20] Stephen Biagi. *Magboltz - transport of electrons in gas mixtures*. URL: <https://magboltz.web.cern.ch/magboltz/>.

-
- [21] I. B. Smirnov. “Modeling of ionization produced by fast charged particles in gases”. *Nuclear Instruments and Methods in Physics Research Section A: Accelerators, Spectrometers, Detectors and Associated Equipment* 554 (2005), pp. 474–493. doi: 10.1016/j.nima.2005.08.064.
- [22] James F. Ziegler. *SRIM - The Stopping and Range of Ions in Matter*. URL: <http://www.srim.org/>.
- [23] Moritz Seidel. “Microscopic Simulation of GEM Signals”. PhD thesis. RWTH Aachen University, Aug. 2018. URL: https://web.physik.rwth-aachen.de/~hebbeker/theses/seidel_bachelor.pdf.

Appendix A

Derivations

A.1 Bohr's Derivation of Energy Loss of Heavy Particles in Matter

Bohr derived the energy loss that an incident particle would experience when it traverses through some material medium. Let us say the incident particle has charge Ze , mass M and is traveling at a velocity v . The mass of an electron is labeled as m_e .

There are two important assumptions that Bohr makes:

1. M is large enough ($M \gg m_e$) that it does not deviate from its path as it goes through the material.
2. The velocity of the incident particle, v , is much greater than that of the velocity of the bound electrons of the atoms in the medium. This assumption is made so that we further safely assume that these bound electrons are stationary with respect to the incident particle.

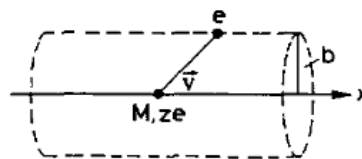


Figure A.1: Schematic diagram of the collision of the incident particle and an electron bound to the atoms of the material. Source: [1]

We now calculate the impulse imparted on an electron at some distance from the incident particle. The distance between these two particles along the Z-direction is b , and can be seen in Figure A.1.

$$I = \int F dt = e \int E dt = e \int E \frac{dt}{dx} dx = e \int E \frac{dx}{v} = \frac{e}{v} \int E_{\perp} dx$$

where E is the total electric field of the incident particle and E_{\perp} is the perpendicular component. We do not have the parallel component (E_{\parallel}) because the values of $e \int_{-\infty}^c E_{\parallel} dx$ and $e \int_c^{\infty} E_{\parallel} dx$ are equal and opposite in magnitude. Here c is the X-coordinate of the electron.

Considering an infinitely long cylinder of radius b , with the central axis along the incident particle trajectory. Using Gauss's Law, we get:

$$\int E_{\perp} 2\pi b dx = 4\pi z e \implies \int E_{\perp} dx = \frac{2ze}{b} \implies I = \frac{2ze^2}{bv}$$

Thus the energy gained by the electron, given by $\frac{I^2}{2m_e}$ is:

$$\Delta E(b) = \frac{2z^2 e^4}{m_e v^2 b^2} \quad (\text{A.1})$$

For N_e being the density of electrons in the medium, the incident particle loses energy to electrons present at a perpendicular distance between b to $b + db$ in a thickness dx given by:

$$-dE(b) = \Delta E(b) N_e dV = \frac{4\pi z^2 e^4}{m_e v^2} N_e \frac{db}{b} dx \implies -\frac{dE}{dx} = \frac{4\pi z^2 e^4 n}{m v^2} \ln \frac{b_{\max}}{b_{\min}}$$

Instead of integrating the above quantity from $b_{\min} = 0$ to $b_{\max} = \infty$ is a wrong direction to proceed in. This is because, for very large b , the collisions do not occur instantly, thus making the impulse calculations invalid. Additionally, the above equation becomes infinite after setting $b_{\min} = 0$.

To obtain the lower limits of the integration b_{\min} , we consider the maximum energy transfer possible in a head-on collision. This corresponds to the electron obtaining energy of $\frac{1}{2}m_e(2v)^2$, which can be derived from the kinematic calculations of elastic collisions between a massive particle and a particle with much lower mass. When relativity is taken into account, the value has to be changed to $2\gamma^2 m v^2$, where $\frac{v}{c}$ and $\gamma = \frac{1}{\sqrt{1-\beta^2}}$. Plugging this loss in energy in Equation A.1, we get:

$$b_{\min} = \frac{ze^2}{\gamma m_e v^2}$$

To calculate the value of b_{\max} , we consider the orbital frequency ν of the bound electrons in the medium. As explained in [1], the impulse transfer should happen in a short time compared to the time period of the bound electron, $\frac{1}{\nu}$. For our collisions, the typical interaction time is given by $t = \frac{b}{v}$, which after accounting for relativity, becomes $\frac{b}{\gamma v}$, so that

$$\frac{b}{\gamma v} \leq \tau = \frac{1}{\bar{\nu}}$$

Considering that there are several bound electrons with different frequencies, we have replaced ν with the mean frequency, $\bar{\nu}$.

Thus, substituting b_{\max} and b_{\min} , we get the Bohr's classical formula:

$$-\frac{dE}{dx} = \frac{4\pi z^2 e^4}{m_e v^2} N_e \ln \frac{\gamma^2 m v^3}{z e^2 \bar{\nu}} \quad (\text{A.2})$$

A.2 Interaction Probability and Mean Free Path

Let us consider a slab of matter with thickness x . We want to calculate the probability for the interaction of a particle traveling through this slab containing many interaction centers. As explained in [1], let $P(x)$ be the probability of not having an interaction after a distance x , and $w dx$ be the probability of having an interaction between x and $x + dx$. The probability of not having an interaction between x and $x + dx$ is given by:

$$\begin{aligned} P(x + dx) &= P(x)(1 - w dx) \\ P(x) + \frac{dP}{dx} dx &= P(x) - P(x)w dx \quad (\text{by first order approximation}) \\ \implies dP(x) &= -w P(x) dx \implies P = C \exp(-wx) \end{aligned}$$

where C is a constant of integration. After imposing $P(0) = 1$, we obtain $C = 1$.

The mean distance travelled by the particle without suffering a collision (λ), or generally known as the mean free path can be calculated using $P(x)$ and is thus found using the relation:

$$\lambda = \frac{\int x P(x) dx}{\int P(x) dx} = \frac{1/w^2}{1/w} = \frac{1}{w} \quad (\text{A.3})$$

A.3 Signal Induced in a Proportional Counter

Consider a proportional counter with an anode wire of radius a and a potential V through a resistance R . The outer cylinder of radius b is grounded. The electric field at a radial distance r measured from the axis is given by

$$E(r) = \frac{V}{r \ln\left(\frac{b}{a}\right)}$$

As explained in [2], we will be calculating the pulse shape $V(t)$ due to induced charge resulting from the motion in the electric field of, say, N electron-ion pairs initially formed at the point r_0 .

Before we proceed, we first need to find the induced charge at the anode from the electron collection. The N electrons and ions that were generated will drift in the electric field towards their respective electrodes, which leads to a transient current that will flow in the external circuit. We will calculate the contribution of each type of carrier to the total current from the conservation of energy. Looking at electrons: the rate $d\epsilon/dt$ of energy gained by the electrons is given by: $\frac{d\epsilon}{dt} = NeE \frac{dx}{dt} = -Ne \frac{dV}{dx} \cdot \frac{dx}{dt} = -Ne \frac{dV}{dt}$ where $\frac{dV}{dt}$ is the rate of change of potential at the location of the electrons due to their drift in the electric field, and V and E are the potential and electric field at a point x respectively.

If C is the capacitance of the detector system, the fully charged system has a stored electrostatic energy of $Q^2/2C$. We also know that $\frac{d\epsilon}{dt} = \frac{d}{dt} \left(\frac{Q^2}{2C} \right) = V \cdot i$, where i is the current flowing in the external circuit due to the motion of the electrons.

From these two equations, we can obtain i and the time integral of which will give us (the change in the induced charge at the anode from the electron collection):

$$q^- = \int i \cdot dt = -Ne \cdot \frac{\Delta V}{V} \quad (\text{A.4})$$

where $\frac{\Delta V}{V}$ is the fraction of the total potential on the system, through which the electrons move before collection, and q^- is the induced charge at the central electrode due to the motion of electrons.

The second part of the calculation is to calculate the time (t_e) for electrons to arrive at

the central wire:

$$t_e = \int_{r_0}^a -\frac{dr}{v_e(r)}$$

where v_e is the drift velocity of the electrons.

Equation 3.2 tells us that the electron drift velocity is proportional to $E^{1/2}$, i.e.

$$v_e = \mu \left(\frac{X}{p} \right)^{1/2} = kr^{-1/2}$$

where $k = \mu \left(\frac{V}{p \ln(b/a)} \right)^{1/2}$

Thus, the time for an electron initially at r_0 to arrive at the central wire is given by:

$$t_e = \int_{r_0}^a -\frac{dr}{v_e(r)} = \frac{2}{3k} \left(r_0^{3/2} - a^{3/2} \right)$$

Now we have all information to perform the final calculation. Let us say that the induced charges at the central electrode due to the motion of electrons and positive ions during the time t are q^- and q^+ respectively (such that $0 < t \leq t_e$). Using Equation A.4, we get:

$$q^-(t) = \frac{-Ne \ln \frac{r_0}{r_e}}{\ln \frac{b}{a}}$$

$$q^+(t) = \frac{Ne \ln \frac{r_0}{r_i}}{\ln \frac{b}{a}}$$

where r_e and r_i are the position of electrons and ions at time t , respectively.

For electron collection, we have:

$$q(t_e) = q^-(t_e) + q^+(t_e) = \frac{-Ne}{\ln \frac{b}{a}} \cdot \ln \frac{r_i}{a}$$

$$V(t_e) = \frac{q(t_e)}{C} = \frac{-Ne}{C \ln \frac{b}{a}} \ln \frac{r_i}{a}$$

Since the distance moved by the ions during electron collection is negligibly small, at t_e , $r_i \simeq r_0$. Thus the maximum pulse height reached during electron collection is:

$$V(t_e) \simeq \frac{-Ne}{C \ln \frac{b}{a}} \cdot \ln \frac{r_0}{a}$$

Appendix B

The Code for Simulating the Thick-GEM Detector on Garfield++

Listing B.1: Thick-GEM simulations using Garfield++

```
1 #include <iostream>
2 #include <TApplication.h>
3 #include <fstream>
4
5 #include "Garfield/SolidBox.hh"
6 #include "Garfield/SolidHole.hh"
7 #include "Garfield/SolidTube.hh"
8 #include "Garfield/SolidRidge.hh"
9 #include "Garfield/GeometrySimple.hh"
10 #include "Garfield/MediumMagboltz.hh"
11 #include "Garfield/MediumConductor.hh"
12 #include "Garfield/MediumPlastic.hh"
13 #include "Garfield/ComponentNeBem3d.hh"
14 #include "Garfield/ViewGeometry.hh"
15 #include "Garfield/ViewField.hh"
16 #include "Garfield/Random.hh"
17 #include "Garfield/Sensor.hh"
18 #include "Garfield/AvalancheMC.hh"
19 #include "Garfield/AvalancheMicroscopic.hh"
20 #include "Garfield/TrackHeed.hh"
21 #include "Garfield/ViewDrift.hh"
22 #include "Garfield/ViewSignal.hh"
```

```
23
24 using namespace std;
25 using namespace Garfield;
26
27 int main(int argc, char * argv[]) {
28
29     TApplication app("app", &argc, argv);
30
31     // Define materials
32     // Gas mixture
33     MediumMagboltz *gas = new MediumMagboltz();
34     const double pressure = 760.;
35     const double temperature = 293.15;
36     gas->SetTemperature(temperature);
37     gas->SetPressure(pressure);
38     gas->SetComposition("Ar", 80., "CO2", 20.);
39     gas->LoadGasFile("../ar_80_co2_20_80k.gas");
40
41
42     // Read the ion mobility table from file.
43     //const string garfpath = getenv("GARFIELD_HOME");
44     gas->LoadIonMobility("/home/garfieldpp/Data/IonMobility_Ar+Ar.txt");
45
46     // Other mediums
47     MediumConductor Cu;
48     MediumPlastic kp;
49     kp.SetDielectricConstant(3.9);
50
51     // Geometry.
52     GeometrySimple geo;
53     geo.SetMedium(gas);
54
55     double i_dia = 0.0200;
```

```

56 double o_dia = 0.0300;
57 double pitch = 0.0600;
58 double vpitch = sqrt(3)*pitch/2, hpitch = pitch/2;
59 double cu_height = 0.0005;
60 double kp_height = 0.0250;
61 double drift_gap = 0.5;
62 double ind_gap = 0.25;
63
64 double anode_z = 0.0 + cu_height/2;
65 double drift_z = anode_z + ind_gap + 2*cu_height +
    ↪ kp_height + drift_gap + cu_height;
66 double cu_upper_z = anode_z + ind_gap + cu_height +
    ↪ kp_height + cu_height;
67 double kapton_z = anode_z + ind_gap + cu_height +
    ↪ kp_height/2 + cu_height/2;
68 double cu_lower_z = anode_z + ind_gap + cu_height;
69
70 double position_x[3] = {-pitch, 0.0, pitch};
71 double position_y[3] = {-pitch, 0.0, pitch};
72
73 double driftV = -2500;
74 double upperV = -1500;
75 double lowerV = -500;
76 double anodeV = 0;
77 double field = (lowerV-upperV)/25;
78
79 double offset_x = 0.0, offset_y = 0.0, offset_z =
    ↪ 0.0; //cu_height/2 + kp_height/2;
80 double offset_x1 = -hpitch/2, offset_y1 = -vpitch/2,
    ↪ offset_z1 = 0.0;
81 double offset_x2 = +hpitch/2, offset_y2 = -vpitch/2,
    ↪ offset_z2 = 0.0;

```

```
82  double offset_x3 = +hpitch/2, offset_y3 = +vpitch/2,
    ↪ offset_z3 = 0.0;
83  double offset_x4 = -hpitch/2, offset_y4 = +vpitch/2,
    ↪ offset_z4 = 0.0;
84
85  std::cout<<"\nPitch = "<<pitch<<endl;
86
87  SolidBox drift(0.0, 0.0, drift_z, hpitch, vpitch,
    ↪ cu_height/2);
88  drift.SetBoundaryPotential(driftV);
89  geo.AddSolid(&drift, &Cu);
90
91
92
93  SolidHole cu_upper(0.0 + offset_x1, 0.0 + offset_y1,
    ↪ cu_upper_z, o_dia/2, o_dia/2, hpitch/2, vpitch/2,
    ↪ cu_height/2);
94  cu_upper.SetBoundaryPotential(upperV);
95  geo.AddSolid(&cu_upper, &Cu);
96
97  SolidHole kapton(0.0 + offset_x1, 0.0 + offset_y1,
    ↪ kapton_z, i_dia/2, i_dia/2, hpitch/2, vpitch/2,
    ↪ kp_height/2);
98  kapton.SetBoundaryDielectric();
99  geo.AddSolid(&kapton, &kp);
100
101  SolidHole cu_lower(0.0 + offset_x1, 0.0 + offset_y1,
    ↪ cu_lower_z, o_dia/2, o_dia/2, hpitch/2, vpitch/2,
    ↪ cu_height/2);
102  cu_lower.SetBoundaryPotential(lowerV);
103  geo.AddSolid(&cu_lower, &Cu);
104
105
```

```

106
107 SolidBox cu_upper2(0.0 + offset_x2, 0.0 + offset_y2,
    ↪ cu_upper_z, hpitch/2, vpitch/2, cu_height/2);
108 cu_upper2.SetBoundaryPotential(upperV);
109 geo.AddSolid(&cu_upper2, &Cu);
110
111 SolidBox kapton2(0.0 + offset_x2, 0.0 + offset_y2,
    ↪ kapton_z, hpitch/2, vpitch/2, kp_height/2);
112 kapton2.SetBoundaryDielectric();
113 geo.AddSolid(&kapton2, &kp);
114
115 SolidBox cu_lower2(0.0 + offset_x2, 0.0 + offset_y2,
    ↪ cu_lower_z, hpitch/2, vpitch/2, cu_height/2);
116 cu_lower2.SetBoundaryPotential(lowerV);
117 geo.AddSolid(&cu_lower2, &Cu);
118
119
120
121 SolidHole cu_upper3(0.0 + offset_x3, 0.0 + offset_y3,
    ↪ cu_upper_z, o_dia/2, o_dia/2, hpitch/2, vpitch/2,
    ↪ cu_height/2);
122 cu_upper3.SetBoundaryPotential(upperV);
123 geo.AddSolid(&cu_upper3, &Cu);
124
125 SolidHole kapton3(0.0 + offset_x3, 0.0 + offset_y3,
    ↪ kapton_z, i_dia/2, i_dia/2, hpitch/2, vpitch/2,
    ↪ kp_height/2);
126 kapton3.SetBoundaryDielectric();
127 geo.AddSolid(&kapton3, &kp);
128
129 SolidHole cu_lower3(0.0 + offset_x3, 0.0 + offset_y3,
    ↪ cu_lower_z, o_dia/2, o_dia/2, hpitch/2, vpitch/2,
    ↪ cu_height/2);

```

```
130 cu_lower3.SetBoundaryPotential(lowerV);
131 geo.AddSolid(&cu_lower3, &Cu);
132
133
134
135 SolidBox cu_upper4(0.0 + offset_x4, 0.0 + offset_y4,
    ↪ cu_upper_z, hpitch/2, vpitch/2, cu_height/2);
136 cu_upper4.SetBoundaryPotential(upperV);
137 geo.AddSolid(&cu_upper4, &Cu);
138
139 SolidBox kapton4(0.0 + offset_x4, 0.0 + offset_y4,
    ↪ kapton_z, hpitch/2, vpitch/2, kp_height/2);
140 kapton4.SetBoundaryDielectric();
141 geo.AddSolid(&kapton4, &kp);
142
143 SolidBox cu_lower4(0.0 + offset_x4, 0.0 + offset_y4,
    ↪ cu_lower_z, hpitch/2, vpitch/2, cu_height/2);
144 cu_lower4.SetBoundaryPotential(lowerV);
145 geo.AddSolid(&cu_lower4, &Cu);
146
147
148
149 SolidBox Anode(offset_x, offset_y, offset_z + anode_z,
    ↪ hpitch, vpitch, cu_height/2);
150 Anode.SetBoundaryPotential(anodeV);
151 Anode.SetLabel("anode");
152 geo.AddSolid(&Anode, &Cu);
153
154
155 //=====
156
157
158 // Plot device geometry in 3D
```

```

159  /*ViewGeometry geomView;
160  geomView.SetGeometry(&geo);
161  geomView.Plot();
162  app.Run();    // Keep this on to interact with the 3D
    ↪ figure
163  */
164
165  // Plot device geometry in 2D
166  /*
167  ViewGeometry geomView2d;
168  geomView2d.SetGeometry(&geo);
169  geomView2d.SetArea(-2*pitch, -2*pitch, -10*kp_height,
    ↪ 2*pitch, 2*pitch, 5*kp_height);
170  geomView2d.SetPlane(0, 1, 0, 0, 0, 0.0);
171  geomView2d.Plot2d();
172  */
173
174  double tgtElSize = 1.e-2; // target element size -3
175  int minEl = 3, maxEl = 8; // minimum and maximum number
    ↪ of elements 3,11
176  int xcopy = 20, ycopy = 20, zcopy = 0;    // no. of
    ↪ copies in the 3 directions
177  ComponentNeBem3d nebem;
178  nebem.SetGeometry(&geo);
179  nebem.SetNumberOfThreads(32); // Set no. of threads for
    ↪ the calculation
180  nebem.SetTargetElementSize(tgtElSize);
181  nebem.SetMinMaxNumberOfElements(minEl, maxEl);
182  nebem.SetPeriodicityX(2*hpitch);
183  nebem.SetPeriodicityY(2*vpitch);
184  nebem.SetPeriodicCopies(xcopy, ycopy, zcopy);
185  nebem.UseLUInversion();
186  //  nebem.EnableDebugging();

```

```
187     nebem.Initialise();
188
189
190     cout<<endl<<"i_dia = "<<i_dia;
191     cout<<endl<<"o_dia = "<<o_dia;
192     cout<<endl<<"pitch = "<<pitch;
193     cout<<endl<<"vpitch = "<<vpitch;
194     cout<<endl<<"cu_height = "<<cu_height;
195     cout<<endl<<"kp_height = "<<kp_height;
196     cout<<endl<<"drift_gap = "<<drift_gap;
197     cout<<endl<<"ind_gap = "<<ind_gap;
198     cout<<endl<<"anode_z = "<<anode_z;
199     cout<<endl<<"drift_z = "<<drift_z;
200     cout<<endl<<"cu_upper_z = "<<cu_upper_z;
201     cout<<endl<<"kapton_z = "<<kapton_z;
202     cout<<endl<<"cu_lower_z = "<<cu_lower_z;
203
204
205
206     int plot_field = 0;
207     int calc_field = 0; // Save electric field/potential
208         ↪ values in a file
209     int calc_ce = 1; // Calculate collection/extraction
210         ↪ efficiency
211     int plot_drift_and_signal = 0; // Plot drift lines of
212         ↪ electrons
213     int gain_calc = 0; // Calculate gain of the detector
214
215     if(plot_field==1){
216         std::cout<<"\n Potential plotting calculations have
217             ↪ begun."<<endl;
218         ViewField fieldView;
219         fieldView.SetComponent(&nebem);
```

```

216     fieldView.SetNumberOfContours(20);
217     // Set the normal vector of the viewing plane (xz
        ↪ plane).
218     fieldView.SetPlane(0, -1, 0, +hpitch/2, +vpitch/2, 0);
219     // Set the plot limits in the current viewing plane.
220     fieldView.SetArea(-2*hpitch, cu_lower_z - 0.01,
        ↪ 2*hpitch, cu_upper_z + 0.01);
221     //fieldView.SetVoltageRange(-80000., 80000.);
222     TCanvas* cf = new TCanvas("cf", "Potential Plot
        ↪ (V/cm)", 600, 500);
223     //cf->SetLeftMargin(0.16);
224     fieldView.SetCanvas(cf);
225     fieldView.PlotContour("v");
226     char name0[1024];
227     sprintf(name0, "Potential_Plot_%dk.pdf", (int)field);
228     cf->SaveAs(name0);
229 }
230
231 if(calc_field==1){
232     std::cout<<"\n Field calculations have begun."<<endl;
233     {// field along line 1
234         std::ofstream fldfile;
235         char name1[1024];
236         sprintf(name1, "%dk_(%d, %d, %d,
            ↪ %d)_20x20_along_x(y=0.5drift_gap).csv",
            ↪ (int)field, (int)anodeV, (int)lowerV,
            ↪ (int)upperV, (int)driftV);
237
238         fldfile.open(name1);
239
240         int nx = 1000;
241         double delx = ((xcopy)*2*hpitch) / (double)(nx - 1);

```

```
242     double xp, yp = offset_y + vpitch/2, zp = offset_z +  
        ↪ cu_upper_z + drift_gap/2;  
243     Medium* medium = nullptr;  
244     double ex = 0., ey = 0., ez = 0., e = 0.0, v = 0.;  
245     int status = 0;  
246     for(int ix = 0; ix < nx; ++ix){  
247         xp = offset_x - (xcopy/2)*2*hpitch + ix*delx;  
248         nebem.ElectricField(xp, yp, zp, ex, ey, ez, v,  
            ↪ medium, status);  
249         e = (ex*ex + ey*ey + ez*ez);  
250         e = pow(e, 0.5);  
251         fldfile << xp << "," << yp << "," << zp << "," << ex  
            ↪ << "," << ey << "," << ez << "," << e << "," <<  
            ↪ v << "," << medium << "," << status <<  
            ↪ std::endl;  
252     }  
253     fldfile.close();  
254 }  
255  
256 {// field along line 2  
257     std::ofstream fldfile;  
258     char name2[1024];  
259     sprintf(name2, "%dk_(%d, %d, %d,  
        ↪ %d)_20x20_along_x(y=0.1_from_top_foil).csv",  
        ↪ (int)field, (int)anodeV, (int)lowerV,  
        ↪ (int)upperV, (int)driftV);  
260  
261     fldfile.open(name2);  
262  
263     int nx = 1000;  
264     double delx = ((xcopy)*2*hpitch) / (double)(nx - 1);  
265     double xp, yp = offset_y + vpitch/2, zp = offset_z +  
        ↪ cu_upper_z + drift_gap/5;
```



```

266 Medium* medium = nullptr;
267 double ex = 0., ey = 0., ez = 0., e = 0.0, v = 0.;
268 int status = 0;
269 for(int ix = 0; ix < nx; ++ix)
270 {
271     xp = offset_x - (xcopy/2)*2*hpitch + ix*delx;
272     nebem.ElectricField(xp, yp, zp, ex, ey, ez, v,
        ↪ medium, status);
273     e = (ex*ex + ey*ey + ez*ez);
274     e = pow(e, 0.5);
275     fldfile << xp << "," << yp << "," << zp << "," << ex
        ↪ << "," << ey << "," << ez << "," << e << "," <<
        ↪ v << "," << medium << "," << status <<
        ↪ std::endl;
276 }
277 fldfile.close();
278 }
279
280 {// field along line 3
281     std::ofstream fldfile;
282     char name3[1024];
283     sprintf(name3, "%dk_(%d, %d, %d,
        ↪ %d)_20x20_along_x(y=0.05_from_top_foil).csv",
        ↪ (int)field, (int)anodeV, (int)lowerV,
        ↪ (int)upperV, (int)driftV);
284     fldfile.open(name3);
285
286     int nx = 1000;
287     double delx = ((xcopy)*2*hpitch) / (double)(nx - 1);
288     double xp, yp = offset_y + vpitch/2, zp = offset_z +
        ↪ cu_upper_z + drift_gap/10;
289     Medium* medium = nullptr;
290     double ex = 0., ey = 0., ez = 0., e = 0.0, v = 0.;

```

```
291     int status = 0;
292     for(int ix = 0; ix < nx; ++ix)
293     {
294         xp = offset_x - (xcopy/2)*2*hpitch + ix*delx;
295         nebem.ElectricField(xp, yp, zp, ex, ey, ez, v,
296             ↪ medium, status);
297         e = (ex*ex + ey*ey + ez*ez);
298         e = pow(e, 0.5);
299         fldfile << xp << "," << yp << "," << zp << "," << ex
300             ↪ << "," << ey << "," << ez << "," << e << "," <<
301             ↪ v << "," << medium << "," << status <<
302             ↪ std::endl;
303     }
304     fldfile.close();
305 }
306
307 { // field along line 4
308     std::ofstream fldfile;
309     char name4[1024];
310     sprintf(name4, "%dk_(%d, %d, %d,
311         ↪ %d)_20x20_along_x(y=0.02_from_anode).csv",
312         ↪ (int)field, (int)anodeV, (int)lowerV,
313         ↪ (int)upperV, (int)driftV);
314     fldfile.open(name4);
315
316     int nx = 1000;
317     double delx = ((xcopy)*2*hpitch) / (double)(nx - 1);
318     double xp, yp = offset_y + vpitch/2, zp = anode_z +
319         ↪ ind_gap/10;
320     Medium* medium = nullptr;
321     double ex = 0., ey = 0., ez = 0., e = 0.0, v = 0.;
322     int status = 0;
323     for(int ix = 0; ix < nx; ++ix)
```

```

316 {
317     xp = offset_x - (xcopy/2)*2*hpitch + ix*delx;
318     nebem.ElectricField(xp, yp, zp, ex, ey, ez, v,
        ↪ medium, status);
319     e = (ex*ex + ey*ey + ez*ez);
320     e = pow(e, 0.5);
321     fldfile << xp << "," << yp << "," << zp << "," << ex
        ↪ << "," << ey << "," << ez << "," << e << ","
        ↪ << v << "," << medium << "," << status <<
        ↪ std::endl;
322 }
323 fldfile.close();
324 }
325
326
327 { // field along line 5
328     std::ofstream fldfile;
329     char name5[1024];
330     sprintf(name5, "%dk_(%d, %d, %d,
        ↪ %d)_20x20_along_x(y=0.5ind_gap).csv", (int)field,
        ↪ (int)anodeV, (int)lowerV, (int)upperV,
        ↪ (int)driftV);
331     fldfile.open(name5);
332
333     int nx = 1000;
334     double delx = ((xcopy)*2*hpitch) / (double)(nx - 1);
335     double xp, yp = offset_y + vpitch/2, zp = cu_lower_z -
        ↪ ind_gap/2;
336     Medium* medium = nullptr;
337     double ex = 0., ey = 0., ez = 0., e = 0.0, v = 0.;
338     int status = 0;
339     for(int ix = 0; ix < nx; ++ix){
340         xp = offset_x - (xcopy/2)*2*hpitch + ix*delx;

```

```
341     nebem.ElectricField(xp, yp, zp, ex, ey, ez, v,
        ↪ medium, status);
342     e = (ex*ex + ey*ey + ez*ez);
343     e = pow(e, 0.5);
344     fldfile << xp << "," << yp << "," << zp << "," << ex
        ↪ << "," << ey << "," << ez << "," << e << "," <<
        ↪ v << "," << medium << "," << status <<
        ↪ std::endl;
345     }
346     fldfile.close();
347 }
348
349 {// field along line 6
350     std::ofstream fldfile;
351     char name6[1024];
352     sprintf(name6, "%dk_(%d, %d, %d,
        ↪ %d)_20x20_along_x(y=0.05_from_bottom_foil).csv",
        ↪ (int)field, (int)anodeV, (int)lowerV,
        ↪ (int)upperV, (int)driftV);
353     fldfile.open(name6);
354
355     int nx = 1000;
356     double delx = ((xcopy)*2*hpitch) / (double)(nx - 1);
357     double xp, yp = offset_y + vpitch/2, zp = cu_lower_z -
        ↪ ind_gap/4;
358     Medium* medium = nullptr;
359     double ex = 0., ey = 0., ez = 0., e = 0.0, v = 0.;
360     int status = 0;
361     for(int ix = 0; ix < nx; ++ix)
362     {
363         xp = offset_x - (xcopy/2)*2*hpitch + ix*delx;
364         nebem.ElectricField(xp, yp, zp, ex, ey, ez, v,
            ↪ medium, status);
```

```

365     e = (ex*ex + ey*ey + ez*ez);
366     e = pow(e, 0.5);
367     fldfile << xp << "," << yp << "," << zp << "," << ex
        ↪ << "," << ey << "," << ez << "," << e << "," <<
        ↪ v << "," << medium << "," << status <<
        ↪ std::endl;
368 }
369 fldfile.close();
370 }
371
372
373 { // field along line 7
374     std::ofstream fldfile;
375     char name7[1024];
376     sprintf(name7, "%dk_(%d, %d, %d,
        ↪ %d)_20x20_along_z.csv", (int)field, (int)anodeV,
        ↪ (int)lowerV, (int)upperV, (int)driftV);
377     fldfile.open(name7);
378
379     int nz = 1000;
380     double delz = (drift_z - anode_z) / (double)(nz - 1);
381     double xp = offset_x + hpitch/2, yp = offset_y +
        ↪ vpitch/2, zp;
382     Medium* medium = nullptr;
383     double ex = 0., ey = 0., ez = 0., e = 0.0, v = 0.;
384     int status = 0;
385     for(int iz = 0; iz < nz; ++iz)
386     {
387         zp = offset_z + anode_z + iz*delz;
388         nebem.ElectricField(xp, yp, zp, ex, ey, ez, v,
            ↪ medium, status);
389         e = (ex*ex + ey*ey + ez*ez);
390         e = pow(e, 0.5);

```

```
391     fldfile << xp << "," << yp << "," << zp << "," << ex  
        ↪ << "," << ey << "," << ez << "," << e << "," <<  
        ↪ v << "," << medium << "," << status <<  
        ↪ std::endl;  
392 }  
393 fldfile.close();  
394 }  
395 }  
396  
397  
398 if(calc_ce == 1){  
399     cout<<"\n Collection Efficiency calulcations have  
        ↪ begun.\n";  
400     int sensor_range = 5;  
401     double xmin = -sensor_range * 2 * hpitch, ymin =  
        ↪ -sensor_range * 2 * vpitch, zmin = 0.0;  
402     double xmax = sensor_range * 2 * hpitch, ymax =  
        ↪ sensor_range * 2 * vpitch, zmax = cu_upper_z +  
        ↪ drift_gap;  
403     // Create the sensor.  
404     Sensor* sensor = new Sensor();  
405     sensor->AddComponent(&nebem);  
406     sensor->SetArea(xmax, ymax, zmax, xmin, ymin, zmin);  
407     //sensor->AddElectrode(&nebem, "anode");  
408     //sensor->AddElectrode(&nebem, "anode2");  
409     std::cout << "Sensor has been created \n";  
410  
411     AvalancheMC aval;  
412     aval.SetSensor(sensor);  
413  
414     /*AvalancheMC drift;  
415     drift.SetSensor(sensor);  
416     drift.SetDistanceSteps(2.e-2);*/
```

```

417
418 //ViewDrift* driftView = new ViewDrift();
419 //constexpr bool plotDrift = false;
420 //if (plotDrift) {
421     //aval.EnablePlotting(driftView);
422     //drift.EnablePlotting(&driftView);
423 //}
424
425 char collection_file[1024];
426 sprintf(collection_file, "CE_%dk_%fcm.csv", (int)field,
    ↪ drift_gap/2);
427 std::ofstream file;
428 file.open(collection_file);
429 file << "Event" << "," << "np" << "," << "j" << "," <<
    ↪ "xe1" << "," << "ye1" << "," << "ze1" << "," <<
    ↪ "xe2" << "," << "ye2" << "," << "ze2" <<
    ↪ std::endl;
430
431 int total = 0, up = 0, down = 0;
432
433 constexpr unsigned int nEvents = 1000;
434 for (unsigned int i = 0; i < nEvents; ++i) {
435     std::cout << "\n " << i+1 << "/" << nEvents << "\n";
436     const double x0 = offset_x3;
437     const double y0 = offset_y3;
438     const double z0 = cu_upper_z + drift_gap/2;
439     const double t0 = 0.;
440     const double e0 = 0.1;
441     aval.AvalancheElectron(x0, y0, z0, t0);
442     file << 0 << "," << 0 << "," << 0 << "," << x0 << ","
        ↪ << y0 << "," << z0 << "," << 0. << "," << 0. <<
        ↪ "," << 0. << std::endl;
443     unsigned int ne = 0, ni = 0;

```

```
444     aval.GetAvalancheSize(ne, ni);
445     cout<<"\n Event = "<<i+1<<" , Avalanche Size
        ↳ (electrons, ions) = ("<<ne<<" , "<<ni<<")\n";
446     const unsigned int np =
        ↳ aval.GetNumberOfElectronEndpoints();
447     double xe1, ye1, ze1, te1, e1;
448     double xe2, ye2, ze2, te2, e2;
449     double xi1, yi1, zi1, ti1;
450     double xi2, yi2, zi2, ti2;
451     int status;
452     for (unsigned int j = 0; j < np; ++j) {
453         aval.GetElectronEndpoint(j, xe1, ye1, ze1, te1,
        ↳ xe2, ye2, ze2, te2, status);
454         file << i << "," << np << "," << j << "," << xe1 <<
        ↳ "," << ye1 << "," << ze1 << "," << xe2 << ","
        ↳ << ye2 << "," << ze2 << std::endl;
455         if(ze1 > kapton_z){
456             total = total + 1;
457             if(ze2 > kapton_z){
458                 up = up + 1;}
459             else if(ze2 < cu_lower_z - ind_gap/10){
460                 down = down + 1;}
461         }
462         //drift.DriftIon(xe1, ye1, ze1, te1);
463         //drift.GetIonEndpoint(0, xi1, yi1, zi1, ti1, xi2,
        ↳ yi2, zi2, ti2, status);
464     }
465     cout<<"\nTotal = "<<total<<"\nUp = "<<up<<"\nDown =
        ↳ "<<down;
466 }
467
468     cout<<"\n::FINAL:: Total = "<<total<<"\nUp =
        ↳ "<<up<<"\nDown = "<<down;
```

```

469     file << total << "," << up << "," << down << "," << 0
        ↪ << "," << 0 << "," << 0 << "," << 0 << "," << 0
        ↪ << "," << 0 << std::endl;
470     //driftView->SetArea(xmax, ymax, zmax, xmin, ymin,
        ↪ zmin);
471     //driftView->SetPlane(0., -1., 0., 0., 0., 0.);
472     //TCanvas* cd = new TCanvas();
473     //driftView->SetCanvas(cd);
474     //driftView->Plot(0);
475     //cd->SaveAs("driftLines.pdf");
476     file.close();
477 }
478
479
480 if(plot_drift_and_signal == 1){
481     int sensor_range = 3;
482     double xmin = -sensor_range * 2 * hpitch, ymin =
        ↪ -sensor_range * 2 * vpitch, zmin = 0.0;
483     double xmax = sensor_range * 2 * hpitch, ymax =
        ↪ sensor_range * 2 * vpitch, zmax = cu_upper_z +
        ↪ drift_gap/5;
484     // Create the sensor.
485     Sensor* sensor = new Sensor();
486     sensor->AddComponent(&nebem);
487     sensor->SetArea(xmax, ymax, zmax, xmin, ymin, zmin);
488     sensor->AddElectrode(&nebem, "anode");
489     sensor->AddElectrode(&nebem, "anode2");
490     std::cout << "Sensor has been created \n";
491
492     // Create the charge multiplication method
493     AvalancheMC* avalMC = new AvalancheMC();
494     avalMC->SetSensor(sensor);
495     avalMC->EnableAvalancheSizeLimit(150);

```

```
496     avalMC->SetDistanceSteps(); // Use lower value for
      ↪ better precision
497     //avalMC->EnableSignalCalculation();
498
499     // HEED
500     TrackHeed* track = new TrackHeed();
501     track->SetSensor(sensor);
502     track->EnableElectricField();
503     track->SetParticle("mu"); // Incident particle
504     track->SetKineticEnergy(1.0e9); // Kinetic energy of
      ↪ the particle in eV
505
506     ViewDrift* driftView = new ViewDrift();
507     driftView->SetArea(xmax, ymax, cu_upper_z + 0.01, xmin,
      ↪ ymin, zmin);
508     driftView->SetPlane(0., -1., 0., 0., vpitch/2, 0.);
509     avalMC->EnablePlotting(driftView);
510     track->EnablePlotting(driftView);
511     TCanvas* cd = new TCanvas();
512     driftView->SetCanvas(cd);
513
514     const double tMin = 0.; // in ns
515     const double tMax = 100.; // in ns
516     const double tStep = 0.05; // in ns
517     const int nTimeBins = int((tMax - tMin) / tStep);
518     sensor->SetTimeWindow(tMin, tStep, nTimeBins);
519
520     float time[nTimeBins], current[nTimeBins];
521
522     // The initial position of the incoming ionizing track
523     double track_x = offset_x3;
524     double track_y = offset_y3;
525     double track_z = cu_upper_z + drift_gap/10;
```

```

526
527     double t0 = 0;
528     double e0 = 0.1;
529     // Momentum direction of incoming track
530     float track_dx = 0.0;
531     float track_dy = 0.0;
532     float track_dz = -1.0;
533
534     int nEvent=3;
535
536     // Cluster info
537     double xcls, ycls, zcls, tcls, ecls, extra;
538     unsigned int ne, ni; // number of electrons in cluster
539     int nel, nend=0;
540     // Electron info
541     double xele, yele, zele, tele, eeel, dxele, dyele,
542           ↪ dzele;
543     int clust_id;
544
545     //If this drift plotting function does not work, start
546     ↪ from the file with commit message "Checked drift
547     ↪ lines for only-MC".
548
549     for(Int_t iEvent=0; iEvent<nEvent;iEvent++){
550         sensor->ClearSignal(); // Reset signals and free
551         ↪ the sensor
552         track->NewTrack(track_x, track_y, track_z, tMin,
553             ↪ track_dx, track_dy, track_dz); // Incident
554         ↪ particle track
555         bool clust_present=0;
556         clust_id = 0;
557         int p = 0;

```

```

552     do{      // Loop over all the cluster positions along
           ↪ the track
553         cout<<"Event = "<<iEvent+1<<": "<<"Cluster =
           ↪ "<<clust_id+1<<" :"<<endl;
554         clust_present=track->GetCluster(xcls, ycls, zcls,
           ↪ tcls, nel, ecl, extra);
555         p = p + nel;
556         for(int j = 0; j < nel; j++){      // Loop over all
           ↪ electrons in a cluster
557             track->GetElectron(j, xele, yele, zele, tele,
           ↪ eeel, dxel, dyel, dzel);
558             avalMC->AvalancheElectron(xele, yele, zele, tele);
559             cout<<"\t j= "<<j+1<<"/"<<nel<<endl;
560         }
561         constexpr bool twod = true;
562         driftView->Plot(0);
563         //driftView->Plot(1);
564         //cd->Modified();
565         clust_id++;
566     }while(clust_present!=0);
567
568     int end=avalMC->GetNumberOfElectronEndpoints();
569     cout<<"\n Gain = "<<end<<endl;
570     cd->SaveAs("driftLines.pdf");
571     //driftView->Clear();
572 }
573 }
574
575 if(gain_calc == 1){
576     int sensor_range = 5;
577     double xmin = -sensor_range * 2 * hpitch, ymin =
           ↪ -sensor_range * 2 * vpitch, zmin = 0.0;

```

```

578     double xmax = sensor_range * 2 * hpitch, ymax =
        ↳ sensor_range * 2 * vpitch, zmax = cu_upper_z +
        ↳ drift_gap/4;
579     // Create the sensor.
580     Sensor* sensor = new Sensor();
581     sensor->AddComponent(&nebem);
582     sensor->SetArea(xmax, ymax, zmax, xmin, ymin, zmin);
583     //sensor->AddElectrode(&nebem, "anode");
584     //sensor->AddElectrode(&nebem, "anode2");
585     std::cout << "Sensor has been created \n";
586
587     // Create the charge multiplication method
588     AvalancheMC* avalMC = new AvalancheMC();
589     avalMC->SetSensor(sensor);
590     //avalMC->EnableAvalancheSizeLimit(150);
591     //avalMC->SetDistanceSteps();    // Use lower value for
        ↳ better precision
592     //avalMC->EnableSignalCalculation();
593
594     // The initial position of the incoming ionizing track
595     double track_x = offset_x3;
596     double track_y = offset_y3;
597     double track_z = cu_upper_z + drift_gap/5;
598
599     double t0 = 0;
600     double e0 = 0.1;
601     // Momentum direction of incoming track
602     float track_dx = 0.0;
603     float track_dy = 0.0;
604     float track_dz = -1.0;
605
606     int nEvent=1000;
607

```

```
608 // Cluster info
609 double xcls, ycls, zcls, tcls, ecl, extra;
610 unsigned int ne, ni; // number of electrons in cluster
611 int nend=0;
612 // Electron info
613 double xele, yele, zele, tele, ee, dxe, dye,
    ↪ dze;
614 int clust_id;
615
616 std::ofstream file;
617 char gain_file[1024];
618 sprintf(gain_file, "Gain_%dk_%fcm.csv", (int)field,
    ↪ drift_gap/5);
619 file.open(gain_file);
620
621 for(Int_t iEvent=0; iEvent<nEvent;iEvent++){
622     avalMC->AvalancheElectron(track_x, track_y, track_z,
    ↪ t0, false);
623     ne = 0;
624     ni = 0;
625     avalMC->GetAvalancheSize(ne, ni);
626     nend = avalMC->GetNumberOfElectronEndpoints();
627     std::cout<<"\n\nEvent: "<<iEvent+1;
628     std::cout<<"\n\nGain from GetAvalSize(): "<<ne;
629     std::cout<<"\n\nGain from GetNo.ofEndpoints():
    ↪ "<<nend<<endl<<endl;
630     file << iEvent+1 << "," << ne << "," << nend <<
    ↪ std::endl;
631 }
632 file.close();
633 }
634
635 cout<<"\n\n :: Complete :: \n\n";
```

```
636     app.Run();  
637     return 0;  
638 }
```

Appendix C

The Code for Simulating the Proportional Counter

Listing C.1: Proportional counter simulations using Garfield++

```
1
2 #include <iostream>
3 #include <TApplication.h>
4 #include <fstream>
5
6 #include "Garfield/SolidBox.hh"
7 #include "Garfield/SolidHole.hh"
8 #include "Garfield/SolidTube.hh"
9 #include "Garfield/SolidWire.hh"
10 #include "Garfield/GeometrySimple.hh"
11 #include "Garfield/MediumMagboltz.hh"
12 #include "Garfield/MediumConductor.hh"
13 #include "Garfield/MediumPlastic.hh"
14 #include "Garfield/ComponentNeBem3d.hh"
15 #include "Garfield/ViewGeometry.hh"
16 #include "Garfield/ViewField.hh"
17 #include "Garfield/Random.hh"
18 #include "Garfield/Sensor.hh"
19 #include "Garfield/AvalancheMC.hh"
20 #include "Garfield/AvalancheMicroscopic.hh"
21 #include "Garfield/TrackHeed.hh"
22 #include "Garfield/ViewDrift.hh"
```

```

23 #include "Garfield/ViewSignal.hh"
24
25 using namespace std;
26 using namespace Garfield;
27
28 int main(int argc, char * argv[]) {
29
30     TApplication app("app", &argc, argv);
31
32     // Define materials
33     // Gas mixture
34     MediumMagboltz *gas = new MediumMagboltz();
35     const double pressure = 760.;
36     const double temperature = 293.15;
37     gas->SetTemperature(temperature);
38     gas->SetPressure(pressure);
39     gas->SetComposition("Ar", 80., "CO2", 20.);
40     gas->LoadGasFile("../ar_80_co2_20_80k.gas");
41
42
43     // Read the ion mobility table from file.
44     const string garfpath = getenv("GARFIELD_HOME");
45     gas->LoadIonMobility(garfpath +
46         ↪ "/Data/IonMobility_Ar+_Ar.txt");
47
48     // Other mediums
49     MediumConductor Cu;
50     MediumPlastic kp;
51     kp.SetDielectricConstant(3.9);
52
53     // Geometry.
54     GeometrySimple geo;
55     geo.SetMedium(gas);

```

```
55
56 double i_dia = 0.027;
57 double o_dia = 1.9;
58 double length = 15;
59
60 double anode_z = 0.0;
61
62 double cathodeV = 0;
63 double anodeV = 2800;
64 double field = (anodeV-cathodeV)/o_dia;
65
66 double offset = 0.01;
67
68 /*SolidHole tube(0.0, 0.0, 0.0, o_dia/2, o_dia/2, o_dia/2
    ↪ + offset, o_dia/2 + offset, length/2);
69 tube.SetBoundaryPotential(cathodeV);
70 geo.AddSolid(&tube, &Cu);*/
71
72 SolidBox box1(o_dia/2, 0.0, 0.0, offset, o_dia/2-offset,
    ↪ length/2);
73 box1.SetBoundaryPotential(cathodeV);
74 geo.AddSolid(&box1, &Cu);
75
76 SolidBox box2(-o_dia/2, 0.0, 0.0, offset, o_dia/2-offset,
    ↪ length/2);
77 box2.SetBoundaryPotential(cathodeV);
78 geo.AddSolid(&box2, &Cu);
79
80 SolidBox box3(0.0, o_dia/2, 0.0, o_dia/2, offset,
    ↪ length/2);
81 box3.SetBoundaryPotential(cathodeV);
82 geo.AddSolid(&box3, &Cu);
83
```

```

84     SolidBox box4(0.0, -o_dia/2, 0.0, o_dia/2, offset,
      ↪ length/2);
85     box4.SetBoundaryPotential(cathodeV);
86     geo.AddSolid(&box4, &Cu);
87
88     SolidTube wire(0.0, 0.0, 0.0, i_dia/2, length/2, 0.0,
      ↪ 0.0, 1.0);
89     wire.SetBoundaryPotential(anodeV);
90     wire.SetLabel("anode");
91     geo.AddSolid(&wire, &Cu);
92
93     //=====
94
95
96     // Plot device geometry in 3D
97     /*ViewGeometry geomView;
98     geomView.SetGeometry(&geo);
99     geomView.Plot();
100    app.Run();    // Keep this on to interact with the 3D
      ↪ figure
101    */
102
103    // Plot device geometry in 2D
104    /*
105    ViewGeometry geomView2d;
106    geomView2d.SetGeometstry(&geo);
107    geomView2d.SetArea(-length, -o_dia, -o_dia, length,
      ↪ o_dia, o_dia);
108    geomView2d.SetPlane(0, -1, 0, 0, 0, 0.0);
109    geomView2d.Plot2d();
110    */
111
112    double tgtElSize = 5.e-3; // target element size -3

```

```
113  int minEl = 3, maxEl = 8; // minimum and maximum number
    ↪ of elements 3,11
114  int xcopy = 0, ycopy = 0, zcopy = 0; // no. of copies in
    ↪ the 3 directions
115  ComponentNeBem3d nebem;
116  nebem.SetGeometry(&geo);
117  nebem.SetNumberOfThreads(8); // Set no. of threads for
    ↪ the calculation
118  nebem.SetTargetElementSize(tgtElSize);
119  nebem.SetMinMaxNumberOfElements(minEl, maxEl);
120  nebem.UseLUInversion();
121  //nebem.EnableDebugging();
122  nebem.Initialise();
123
124
125  int plot_field = 0; // Plot the electric field/potentials
126  int calc_field = 0; // Store the electric field/potential
    ↪ values in a file
127  int plot_drift_and_signal = 0; // Plot the drift lines of
    ↪ electrons
128  int gain_calc = 1; // Calculate gain of the detector
129
130
131  if(plot_field==1){
132      std::cout<<"\n Potential plotting calculations have
    ↪ begun."<<endl;
133
134      ViewField fieldp;
135      fieldp.SetComponent(&nebem);
136      fieldp.PlotProfile(0.0, 0.0, 0.0, o_dia/1.8, 0.0, 0.0,
    ↪ "e", false);
137
138      ViewField fieldView;
```

```

139     fieldView.SetComponent(&nebem);
140     fieldView.SetNumberOfContours(100);
141     // Set the normal vector of the viewing plane (xz
        ↪ plane).
142     fieldView.SetPlane(0, -1, 0, 0.0, 0.0, 0.0);
143     // Set the plot limits in the current viewing plane.
144     fieldView.SetArea(-length/4, -2*o_dia, length/4,
        ↪ 2*o_dia);
145     //fieldView.SetVoltageRange(-80000., 80000.);
146     TCanvas* cf = new TCanvas("cf", "Potential Plot
        ↪ (V/cm)", 600, 500);
147     //cf->SetLeftMargin(0.16);
148     fieldView.SetCanvas(cf);
149     fieldView.PlotContour("e");
150     char name0[1024];
151     sprintf(name0, "Box_tube_Potential_Plot.pdf");
152     cf->SaveAs(name0);
153 }
154
155 if(calc_field==1){
156     std::cout<<"\n Field calculations have begun."<<endl;
157     {// field along line 1
158         std::ofstream fldfile;
159         char name1[1024];
160         sprintf(name1, "Box_tube_(%d, %d)_along_z.csv",
            ↪ (int)anodeV, (int)cathodeV);
161
162         fldfile.open(name1);
163
164         int nx = 1000;
165         double delx = (o_dia/1.8) / (double)(nx - 1);
166         double xp = 0.0, yp = 0.0, zp = 0.0;
167         Medium* medium = nullptr;

```

```
168     double ex = 0., ey = 0., ez = 0., e = 0.0, v = 0.;
169     int status = 0;
170     for(int ix = 0; ix < nx; ++ix){
171         xp = 0.0 + ix*delx;
172         nebem.ElectricField(xp, yp, zp, ex, ey, ez, v,
173             ↪ medium, status);
174         e = (ex*ex + ey*ey + ez*ez);
175         e = pow(e, 0.5);
176         fldfile << xp << "," << yp << "," << zp << "," << ex
177             ↪ << "," << ey << "," << ez << "," << e << "," <<
178             ↪ v << "," << medium << "," << status <<
179             ↪ std::endl;
180     }
181     fldfile.close();
182 }
183
184 if(plot_drift_and_signal == 1){
185
186     // Create the sensor.
187     Sensor* sensor = new Sensor();
188     sensor->AddComponent(&nebem);
189     double xmax = o_dia/2, ymax = o_dia/2, zmax = length/4,
190         ↪ xmin = -o_dia/2, ymin = -o_dia/2, zmin =
191         ↪ -length/4;
192     sensor->SetArea(xmax, ymax, zmax, xmin, ymin, zmin);
193     sensor->AddElectrode(&nebem, "anode");
194     std::cout << "Sensor has been created \n";
195
196     // Create the charge multiplication method
197     AvalancheMC* avalMC = new AvalancheMC();
198     avalMC->SetSensor(sensor);
```

```

195 //avalMC->EnableAvalancheSizeLimit();
196 avalMC->SetDistanceSteps(); // Use lower value for
    ↳ better precision
197 //avalMC->EnableSignalCalculation();
198
199 // HEED
200 TrackHeed* track = new TrackHeed();
201 track->SetSensor(sensor);
202 track->EnableElectricField();
203 track->SetParticle("mu"); // Incident particle
204 track->SetKineticEnergy(1.0e9); // Kinetic energy of
    ↳ the particle in eV
205
206 ViewDrift* driftView = new ViewDrift();
207 driftView->SetArea(xmax, ymax, zmax, xmin, ymin, zmin);
208 driftView->SetPlane(0., -1., 0., 0.0, 0.0, 0.0);
209 avalMC->EnablePlotting(driftView);
210 track->EnablePlotting(driftView);
211 TCanvas* cd = new TCanvas();
212 driftView->SetCanvas(cd);
213
214 const double tMin = 0.; // in ns
215 const double tMax = 100.; // in ns
216 const double tStep = 0.05; // in ns
217 const int nTimeBins = int((tMax - tMin) / tStep);
218 sensor->SetTimeWindow(tMin, tStep, nTimeBins);
219
220 float time[nTimeBins], current[nTimeBins];
221
222 // The initial position of the incoming ionizing track
223 double track_x = o_dia/2.5;
224 double track_y = 0.0;
225 double track_z = 0.0;

```

```
226
227     double t0 = 0;
228     double e0 = 0.1;
229     // Momentum direction of incoming track
230     float track_dx = -1.0;
231     float track_dy = 0.0;
232     float track_dz = 0.0;
233
234     int nEvent=1;
235
236     // Cluster info
237     double xcls, ycls, zcls, tcls, ecls, extra;
238     unsigned int ne, ni; // number of electrons in cluster
239     int nel, nend=0;
240     // Electron info
241     double xele, yele, zele, tele, eele, dxele, dyele,
242           ↪ dzele;
243     int clust_id;
244
245     cout<<"\n\nMedium at mid-drift gap ("<<o_dia/3<<"):
246           ↪ "<<geo.GetMedium(0.0, 0.0, o_dia/3)<<endl<<endl;
247
248     for(Int_t iEvent=0; iEvent<nEvent;iEvent++){
249         sensor->ClearSignal();    // Reset signals and free
250           ↪ the sensor
251         track->NewTrack(track_x, track_y, track_z, tMin,
252           ↪ track_dx, track_dy, track_dz);    // Incident
253           ↪ particle track
254         bool clust_present=0;
255         clust_id = 0;
256         int p = 0;
257         do{    // Loop over all the cluster positions along
258           ↪ the track
```



```

253     cout<<"Event = "<<iEvent+1<<": "<<"Cluster =
        ↳ "<<clust_id+1<<" : "<<endl;
254     clust_present=track->GetCluster(xcls, ycls, zcls,
        ↳ tcls, nel, ecl, extra);
255     p = p + nel;
256     for(int j = 0; j < nel; j++){ // Loop over all
        ↳ electrons in a cluster
257         track->GetElectron(j, xe, ye, ze, te,
            ↳ ee, dx, dy, dz);
258         avalMC->AvalancheElectron(xe, ye, ze, te);
259         cout<<"\t j= "<<j+1<<"/"<<nel<<endl;
260     }
261     constexpr bool twod = true;
262     driftView->Plot(0);
263     //driftView->Plot(1);
264     //cd->Modified();
265     clust_id++;
266     }while(clust_present!=0);
267
268     int end=avalMC->GetNumberOfElectronEndpoints();
269     cout<<"\n Gain = "<<end<<endl;
270     cd->SaveAs("driftLines.pdf");
271     //driftView->Clear();
272 }
273 }
274
275 if(gain_calc == 1){
276     double xmin = -o_dia/2, ymin = -o_dia/2, zmin =
        ↳ -length/4;
277     double xmax = o_dia/2, ymax = o_dia/2, zmax = length/4;
278     // Create the sensor.
279     Sensor* sensor = new Sensor();
280     sensor->AddComponent(&nebem);

```

```
281 sensor->SetArea(xmax, ymax, zmax, xmin, ymin, zmin);
282 //sensor->AddElectrode(&nebem, "anode");
283 //sensor->AddElectrode(&nebem, "anode2");
284 std::cout << "Sensor has been created \n";
285
286 // Create the charge multiplication method
287 AvalancheMC* avalMC = new AvalancheMC();
288 avalMC->SetSensor(sensor);
289 //avalMC->EnableAvalancheSizeLimit(150);
290 //avalMC->SetDistanceSteps(); // Use lower value for
    ↪ better precision
291 //avalMC->EnableSignalCalculation();
292
293 // The initial position of the incoming ionizing track
294 double track_x = o_dia/2.1;
295 double track_y = 0.0;
296 double track_z = 0.0;
297
298 double t0 = 0;
299 double e0 = 0.1;
300 // Momentum direction of incoming track
301 float track_dx = -1.0;
302 float track_dy = 0.0;
303 float track_dz = 0.0;
304
305 int nEvent=1000;
306
307 // Cluster info
308 double xcls, ycls, zcls, tcls, ecls, extra;
309 unsigned int ne, ni; // number of electrons in cluster
310 int nend=0;
311 // Electron info
```

```

312     double xele, yele, zele, tele, eeel, dxele, dyele,
        ↪ dzele;
313     int clust_id;
314
315     std::ofstream file;
316     char gain_file[1024];
317     sprintf(gain_file, "Box_tube_gain_%fcm.csv", track_x);
318     file.open(gain_file);
319
320     for(Int_t iEvent=0; iEvent<nEvent;iEvent++){
321         avalMC->AvalancheElectron(track_x, track_y, track_z,
        ↪ t0, false);
322         ne = 0;
323         ni = 0;
324         avalMC->GetAvalancheSize(ne, ni);
325         nend = avalMC->GetNumberOfElectronEndpoints();
326         std::cout<<"\n\nEvent: "<<iEvent+1;
327         std::cout<<"\n\nGain from GetAvalSize(): "<<ne;
328         std::cout<<"\n\nGain from GetNo.ofEndPoints():
        ↪ "<<nend<<endl<<endl;
329         file << iEvent+1 << "," << ne << "," << nend <<
        ↪ std::endl;
330     }
331     file.close();
332 }
333
334     cout<<"\n\n :: Complete :: \n\n";
335     app.Run();
336     return 0;
337 }

```